Passage of the HIV capsid cracks the nuclear pore

Authors: Jan Philipp Kreysing[1,2,†], Maziar Heidari[3,†], Vojtech Zila[4,†], Sergio Cruz-Leon[3],

Agnieszka Obarska-Kosinska[1], Vibor Laketa[4,5], Sonja Welsch[6], Jürgen Köfinger[3], Beata

Turoňová[1], Gerhard Hummer[3,7]*, Hans-Georg Kräusslich[4,5]*, Martin Beck[1,8]*

[†] Contributed equally

[*] Corresponding authors:

gerhard.hummer@biophys.mpg.de,

hans-georg.kraeusslich@med.uni-heidelberg.de,

martin.beck@biophys.mpg.de

Affiliations:

[1] Department of Molecular Sociology, Max Planck Institute of Biophysics, Max-von-Laue-Straße 3, 60438 Frankfurt am Main, Germany.

[2] IMPRS on Cellular Biophysics, Max-von-Laue-Straße 3, 60438 Frankfurt am Main, Germany.

[3] Department of Theoretical Biophysics, Max Planck Institute of Biophysics, Max-von-Laue-Straße 3, 60438 Frankfurt am Main, Germany.

[4] Department of Infectious Diseases, Virology, Heidelberg University, Heidelberg, Germany.

[5] German Centre for Infection Research (DZIF), Partner Site Heidelberg, Germany

[6] Central Electron Microscopy Facility, Max Planck Institute of Biophysics, Max-von-Laue-Straße 3, 60438, Frankfurt am Main, Germany.

[7] Institute of Biophysics, Goethe University Frankfurt, 60438 Frankfurt am Main, Germany.

[8] Institute of Biochemistry, Goethe University Frankfurt, 60438 Frankfurt am Main, Germany.

Summary

Upon infection, human immunodeficiency virus (HIV-1) releases its cone-shaped capsid into the cytoplasm of infected T-cells and macrophages. As its largest known cargo, the capsid enters the nuclear pore complex (NPC), driven by interactions with numerous FG-repeat nucleoporins (FG-Nups). Whether NPCs structurally adapt to capsid passage and whether capsids are modified during passage remains unknown, however. Here, we combined super-resolution and correlative microscopy with cryo electron tomography and molecular simulations to study nuclear entry of HIV-1 capsids in primary human macrophages. We found that cytosolically bound cyclophilin A is stripped off capsids entering the NPC, and the capsid hexagonal lattice remains largely intact inside and beyond the central channel. Strikingly, the NPC scaffold rings frequently crack during capsid passage, consistent with computer simulations indicating the need for NPC widening. The unique cone shape of the HIV-1 capsid facilitates its entry into NPCs and helps to crack their rings.

Introduction

Human immunodeficiency virus type 1 (HIV-1) is a lentivirus that can infect non-dividing cells including human macrophages [1]. Fusion of the viral and cellular membrane leads to cytoplasmic entry of the characteristic cone-shaped HIV-1 capsid that encases the viral genome and replication machinery. Subsequently, the viral genomic RNA undergoes reverse transcription into double-stranded cDNA, which eventually becomes integrated into the host cell genome, where it is maintained for the life of the infected cell. Reverse transcription initiates in the cytoplasm and is completed after nuclear entry of the subviral replication complex prior to integration into the host cell genome [2-4]. HIV-1 subviral complexes comprise the viral genome associated with nucleocapsid proteins and the replication proteins reverse transcriptase (RT) and integrase (IN). While earlier studies indicated rapid disassembly of the capsid in the cytoplasm releasing the free replication complex, it is now clear that the capsid can be stably maintained up to nuclear entry [5, 6]. During cytoplasmic transit, the HIV-1 capsid has been shown to engage multiple host cell restriction and dependency factors, to serve as a reaction container for reverse transcription and to shield the nascent viral cDNA from cytoplasmic antiviral DNA sensors [5, 6]. Furthermore, the capsid lattice engages microtubular motors, thus facilitating its transport towards the nuclear envelope [7-9]. Capsid also interacts with the cytoplasmic protein cyclophilin A (CypA) [10, 11] and with the Cyp domain of Nup358 at the cytoplasmic side of nuclear pores, potentially docking the capsid to the nuclear pore complex (NPC) [12]. Accordingly, the HIV-1 capsid is the main orchestrator of the early post-entry phase of viral replication.

A potential role of the HIV-1 capsid for nuclear entry and in the nucleoplasm of non-dividing cells has long been under debate [5, 6]. The capsid consists of 200-250 hexamers of the viral CA protein with 12 CA pentamers inserted in regions of high curvature [13-15]. The hexamers have been shown to specifically interact with phenylalanine-glycine (FG) repeats that are present within intrinsically disordered regions of several nucleoporins (FG-Nups) [16, 17]. The FG-binding hydrophobic cleft within the CA hexamer also interacts with an FG-containing motif of the nuclear protein cleavage and polyadenylation specificity factor 6 (CPSF6) [17]. FG-motif containing host factors can be displaced by small molecules (e.g., Lenacapavir [18]), competitively binding the CA pocket [19]. Lenacapavir has recently been approved for treatment of HIV-1 infected patients. The capsid-targeting compounds can block nuclear entry of HIV-1 replication complexes, supporting a role of the capsid during NPC passage [16, 19, 20]. The size

72   discrepancy between the HIV-1 capsid (ca. 60 nm at the broad end [15]) and the inner diameter

73   of NPCs obtained from isolated nuclear envelopes (ca. 45 nm [21]) had led to the conclusion that

74   genome uncoating must occur prior to entry into the NPC channel, possibly leaving some CA

75   remnants on the subviral complex. This hypothesis was supported by the observation that a

76   CypA-DsRed fluorescent fusion protein, which efficiently binds cytoplasmic capsids, was

77   rapidly lost when the fluorescent structure reached the nuclear pore [22]. Recent ultrastructural

78   studies have shown, however, that (largely) intact capsids can enter the nucleus in a T-cell line

79   through apparently normal nuclear pores [23], and cone-shaped capsids encasing electron-dense

80   nucleoprotein complexes have been detected inside the nucleus of HIV-1 infected reporter cell

81   lines and primary human macrophages [23,4,24]. This was explained by the recent observation,

82   that the central channel of NPCs can adapt its diameter in response to forces laterally imposed

83   by the nuclear membranes [25]. With an inner diameter of approximately 45-65 nm [23, 26-28] the

84   NPC central channel of human tissue culture cells appeared to be sufficiently wide for passage

85   of the complete HIV-1 capsid.

86   NPCs consist of three sandwiched rings. The nuclear (NR), inner (IR) and cytoplasmic ring

87   (CR) are 8-fold rotationally symmetric structures that form a central channel thus bridging

88   across the inner and outer membranes of the nuclear envelope. The conformational changes

89   that occur during NPC diameter changes differ markedly between the individual rings. While

90   the CR and NR form an elaborate and thoroughly connected scaffold that is bent during dilation

91   movements, the IR consists of eight spokes that are flexibly connected. These spokes move

92   outwards and away from each other during NPC dilation, thereby stretching their linkers and

93   opening up additional space within the central channel [26, 29]. If and how the dilation of

94   individual NPC is coordinated with the transport of large cargos remains unknown, however.

95   Nuclear transport cargo passes through the central channel, which is filled with tens of

96   megadaltons of intrinsically disordered FG-Nups. These FG-Nups selectively bind cargo to

97   facilitate nuclear import, but at the same time exclude the vast majority of proteins from

98   entering the nucleus [30]. FG-Nups thus form the permeability barrier for the nuclear envelope,

99   protect the host cell genome and constitute a major barrier that would have to be overcome by

100   the HIV-1 capsid for nuclear entry [31]. However, two recent studies showed that in vitro

101   assembled HIV-1 capsids rapidly partitioned into phase separated condensates of the

102   intrinsically disordered FG repeat region of Nup98, and partitioning was dependent on the FG

103   binding pocket in CA [32, 33]. These results confirmed that the viral capsid itself constitutes a

104   multivalent nuclear import cargo with surface properties similar to nuclear transport receptors.

105   Upon reaching the nucleus, the capsid must eventually break open to release the reverse

106   transcribed genome for integration to occur. Although mounting evidence indicates that

107   transcriptional latency, as the main obstacle for HIV-1 cure, is mediated in part by the position

108   of genome integration [34, 35], neither the mechanism nor the regulation of time or place of

109   uncoating are currently understood.

110   The two central questions regarding nuclear import of the HIV-1 capsid are: How do capsids

111   pass through a channel of comparable width that is densely filled with FG-Nups? And further,

112   at what location do capsids open to release the genome? Three scenarios may be considered,

113   which are not mutually exclusive. (i) The capsid lattice may be elastic, a hypothesis that is

114   supported by a recent preprint reporting the capsid lattice to undergo reversible deformation

115   without disintegration [36]. (ii) The capsid lattice may break during NPC passage, thus altering

116   its geometry. While morphologically normal appearing capsids have been detected in the

117   nucleoplasm of non-dividing cells, lattice analysis so far has been performed only on cell-free

118   virions and lattice completeness of intracellular capsids has not been determined. (iii) Passage

119   of the HIV-1 capsid through the NPC channel may induce local NPC dilation, possibly even to

120   a point where the NPC scaffold is altered, thereby giving room for intact capsids to pass.

121   Here, we provide direct evidence for loss of CypA from HIV-1 capsids at the nuclear pore. We

122   show that NPC passage appears rate-limiting in primary human macrophages and we identify

123   apparently intact, nucleic acid-containing capsids in the nucleoplasm of these cells. Most

124   importantly, we provide experimental evidence that passage of intact HIV-1 capsids cracks the

125   NPC architecture. Computational simulation supports a scenario in which cracking of the NPC

126   scaffold facilitates capsid passage by relieving a steric barrier.

127

Results

129

Subviral HIV-1 complexes accumulate at nuclear pores in human primary macrophages

131

132   We studied nuclear entry of subviral HIV-1 complexes in primary human monocyte-derived

133   macrophages (MDM). Macrophages are natural target cells of HIV-1 and are post-mitotic;

134   accordingly, the viral replication complex has to enter the nucleus through the intact nuclear

135   envelope. To analyze this process, we made use of our previously described non-infectious

HIV-1 variant (NNHIV) that carries a complete HIV-1 genome with deleterious mutations in IN and a deletion in the *tat* gene. We have previously shown that NNHIV can enter permissive cells and undergo reverse transcription and nuclear entry similar to wild-type HIV-1, but is defective in integration and gene expression [23].

Freshly prepared MDM were incubated with NNHIV carrying a macrophage-tropic HIV-1 envelope (Env) glycoprotein for different periods of time and fixed cells were immunostained for HIV-1 CA and for lamin A/C to define the nuclear boundary. Using confocal microscopy, we observed significant variability in efficiency of subviral complexes to reach the nucleus between individual cells from one donor as well as between different donors. Some cells exhibited CA signals distributed through the whole cell including nuclear regions, while others did not show any signal in the proximity of or inside the nucleus. Focusing on cells displaying intranuclear HIV-1 signals, we observed a strong enrichment of subviral complexes overlaying the lamin signal and thus likely localized at the nuclear envelope. This phenotype was clearly detected at 24 h post infection (p.i.) and was stronger at 48 h p.i. (Figure 1A-C), while CA signals were cytoplasmically distributed at earlier time points. Starting at 24 h p.i., we observed clear HIV-1 signals in the nucleus of NNHIV-treated MDM and their number increased at 48 h p.i. (Figure 1A-C).

To analyze whether nuclear envelope-associated capsids were enriched at NPCs, we performed stimulated emission depletion (STED) nanoscopy of primary MDM from different donors. Cells were incubated with NNHIV for 48 h and stained for HIV-1 CA and FG-Nups. Subsequently, we performed two-color 3D STED nanoscopy and acquired super-resolved images in sequential optical sections to cover the entire nuclear volume of individual cells. Analysis of computational slices of fully reconstructed MDM nuclei confirmed the direct association of the HIV-1 capsid with nuclear pores (Figure 1D, Video S1). Quantitative analysis showed that 89% (908 of 1,025) of all CA signals detected at the nuclear envelope were closely associated with nuclear pores. These results clearly showed that HIV-1 capsids specifically associate with nuclear pores in infected MDM, and their strong accumulation suggests that passage through the nuclear pore is a rate-limiting event in early HIV-1 replication.
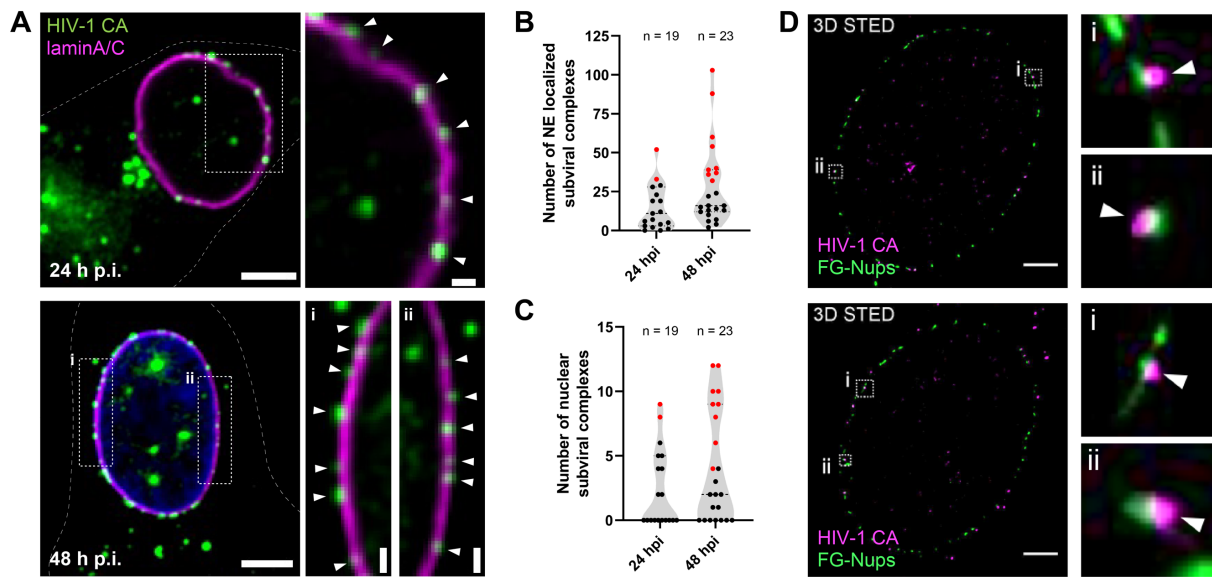
Figure 1. **HIV-1 capsids accumulate at nuclear pores in primary human macrophages**. (A–C) MDM were infected with macrophage-tropic NNHIV for 24 h (A, upper) or 48 h (A, lower). Cells were then fixed, methanol extracted and immunostained for HIV-1 CA (green) and laminA/C (magenta). Shown are confocal z slices through the nuclei of infected MDM. The enlarged regions (A, right) display HIV-1 CA signals (white arrowheads) accumulated at the nuclear envelope (NE) as defined by laminA/C staining. (B, C) Quantification of CA signals representing subviral complexes co-localizing with laminA/C (B) and number of CA signals detected inside the nucleus (C) at indicated times p.i. Indicated in red are values from cells exhibiting >30 CA signals colocalizing with laminA/C. Results represent data obtained by analysis of (n) cells from one representative donor. (D) 3D STED imaging of nuclei of HIV-1 infected MDM. Cells were infected for 48 h, fixed, methanol extracted and immunostained for HIV-1 CA (magenta) and FG-Nups (green). Slices through the 3D reconstruction of an entire nucleus are shown with enlargements (D, right) displaying CA signals (white arrowheads) directly associated with NPCs as defined by FG-Nup staining. See also Video S1. Scale bars: 2 μm.

**HIV-1 capsids are detected upon entry into, passage through and exit from the NPC**

In order to determine the relative positioning of HIV-1 capsids at the nuclear pore, we combined two-color STED nanoscopy for CA and FG-Nups with nuclear Hoechst staining in confocal mode to define the nuclear side. Maximum intensity of the FG repeat immunofluorescence signal is expected to localize to the central channel at the inner ring of the nuclear pore [37]. Analyzing cells at 48 h p.i., we observed CA signals in three positions: at the cytoplasmic side, directly overlapping the FG signal and at the nucleoplasmic side of the nuclear pore (Figure 2A). For quantitative analysis, we segmented individual capsid-associated pores and determined the normalized signal intensities of the FG-Nup and CA signals for a line profile (Figure 2B). This analysis confirmed that HIV-1 capsids could be observed upon their entry into, passage through and exit from the central channel of the NPC

193   in infected MDM. The distribution for these three different positions relative to the center of

194   the nuclear pore was determined for a total of 180 capsid-associated nuclear pores in MDM

195   from three different donors (Figure 2C). A similar distribution was observed for all three

196   donors with 51 % of capsids observed on the cytoplasmic side of the nuclear pore, 33 %

197   overlapping the FG repeat in the central channel and 15 % on the nucleoplasmic side (Figure

198   2C). These results indicated that entry into and passage through the nuclear pore may be

199   delaying or limiting nuclear entry of HIV-1 capsids in MDM. The substantial number of

200   capsids observed at the nucleoplasmic side of NPCs further suggested that release from the

201   nuclear basket may not be instantaneous after passage through the central channel.

202
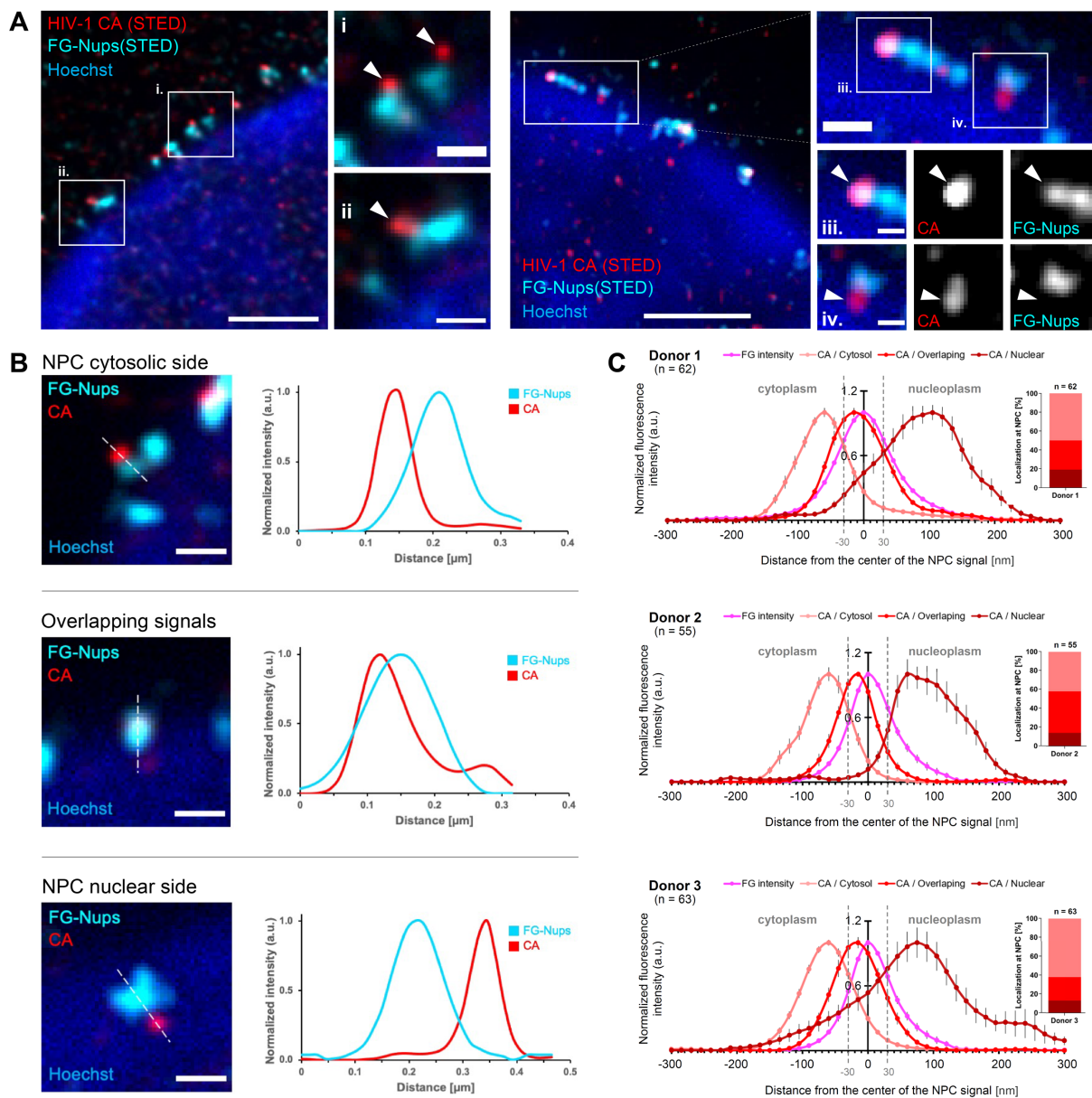
Figure 2. **Super resolution analysis of HIV-1 subviral complexes at nuclear pores of infected MDM**. MDM were infected with NNHIV-1, fixed at 48 h post-infection and immunostained for HIV-1 CA (red) and FG-Nups (cyan). The nuclear region was visualized by staining with Hoechst and analysed in confocal mode (blue). (A) STED microscopy images displaying nuclear segments of two infected MDM. The enlarged regions show CA signals (white arrowheads) at the cytoplasmic side of the NPC (i. and ii.), overlapping CA and NPC signals (iii.), and CA signals located at the nuclear side of the NPC (iv.). (B) Three typical localizations of HIV signals at the NPC with corresponding CA and FG-Nups signal intensity profiles. Graphs show intensities normalized to the respective maximal value measured in line profiles indicated in images on the left. (C) Averaged line profiles measured on (n) nuclear pores with associated CA signals from three independent experiments, each using cells from a different donor. Error bars represent SD. The localization of CA signals at the NPC was classified as cytoplasmic side of the NPC (pink line), overlapping with NPC (red line) or nuclear side of the NPC (dark red line), applying a window of 30 nm distance of the CA intensity peak from the FG-Nups (magenta line) intensity peak (dashed vertical lines). Scale bars: 500 nm.

Subviral complexes passing through the central NPC channel are cone-shaped capsids

The fluorescence imaging results clearly revealed the accumulation of CA containing subviral complexes at and inside nuclear pores of infected MDM, but did not provide sufficient resolution to define the morphology and structure of the cargo. We therefore applied 3D correlative light and electron microscopy (CLEM). MDM were infected with NNHIV carrying a fluorescent fusion protein of the viral IN with mScarlet to identify intracellular subviral HIV-1 complexes. MDM were cryo-immobilized by high pressure freezing at 48 h p.i. and further processed for CLEM. Tilt series were acquired for 61 positions of correlated regions targeting IN.mScarlet signals at nuclear envelope regions (defined by Hoechst staining of resin sections) identified in 17 cells from two donors. From this data set, we identified a total of 43 structures completely covered in the resin sections that resembled HIV-1 capsids inside or immediately adjacent to nuclear pores. Their distribution across the NPC was similar to that observed by STED nanoscopy with 19 subviral particles on the cytoplasmic side, 13 deep inside the NPC and 11 on the nucleoplasmic side (Figure S1). Overall, the morphology of the observed subviral structures closely matched that of mature capsids inside purified HIV-1 particles, including the presence of dense material inside capsid structures indicating the presence of condensed ribonucleoprotein or reverse transcription intermediates (Figure 3 and S1). The majority of structures was cone-shaped (41/43; 95%) with rare tubular structures (2/43; 4.7%) (Figure S1). Capsid-like structures at or within the nuclear pore exhibited an average length of 111 ± 11 nm and an average width of 53 ± 6 nm, similar to the dimensions determined for mature HIV-1 capsids by cryo ET [38], and almost identical to the dimensions observed in our previous CLEM analysis of an infected T-cell line [23]. Importantly, we did not observe apparently empty (lacking

244   dense inner material) or obviously broken capsid-like particles inside or directly associated

245   with the nuclear pore in infected MDM (Fig. S1).

246   Figure 3A depicts CLEM of a strongly fluorescent cluster directly associated with the nuclear

247   border of an infected MDM. A slice through the tomographic reconstruction at the correlated

248   position is shown in Figure 3A". The segmented and isosurface-rendered representation of this

249   region (Figure 3A```) features a total of four cone-shaped and visually intact HIV-1 capsids

250   completely covered in the resin section at different stages of nuclear import (see inserts in

251   Figure 3A`` and supplementary movie 2). All four capsids that had entered into the NPC were

252   oriented with their narrow end first. We sometimes detected capsids positioning their broad end

253   towards the nuclear envelope in the vicinity of nuclear pores (Figure 3A''' left), but this

254   orientation was not observed for particles that had started penetrating the pore.

255   Capsid-like structures deep inside the central channel (Figure 3A) and on the nucleoplasmic

256   side (Figure 3B, C) retained apparently normal cone-shaped morphology (except for one

257   tubular structure) and dense material inside without any obvious defects (Figure S1). All 32

258   capsids inside the central channel were oriented with their narrow end towards the nuclear side

259   (Figure S1). Contrary to expectation, capsids on the nucleoplasmic side were found to be

260   oriented in two orientations at equal frequency: either with their narrow end away from (Figure

261   3B, inset ii) or towards the NPC (Figure 3C) (Figure S1). This result indicated that after passage

262   through the central NPC channel, the HIV-1 capsid remains flexibly attached to the nuclear

263   basket for some time before being released into the nucleoplasm and further trafficking to the

264   site of integration.
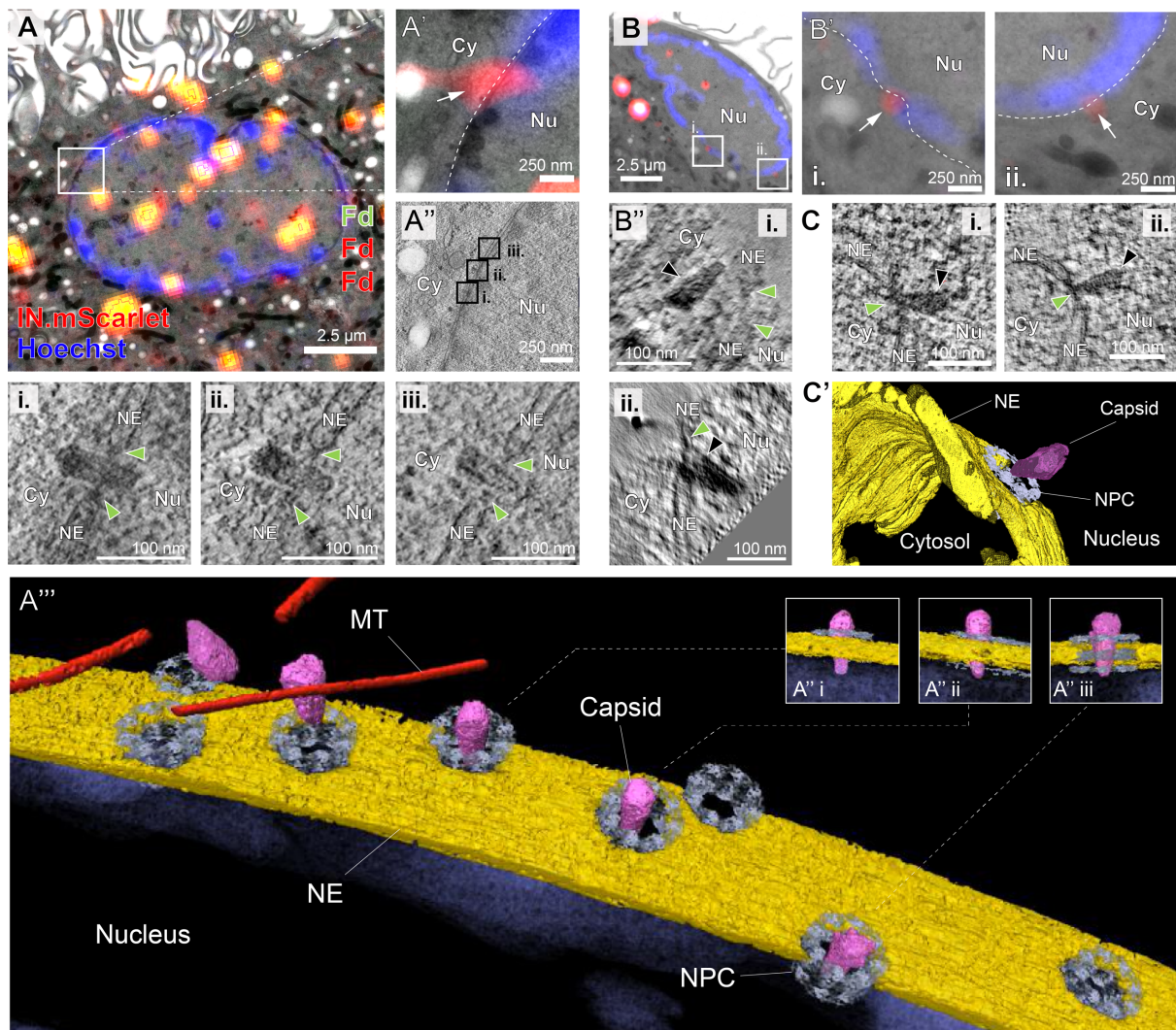
Figure 3. Morphologically intact HIV-1 capsids at and inside NPCs of human MDM.
MDM were infected with macrophage-tropic IN.mScarlet carrying NNHIV for 48 h at 37°C, prior to cryo-immobilization by high pressure freezing, embedding and further processing for CLEM-ET. Fluorescently labelled subviral structures in the region of the nuclear envelope were visualized by CLEM-ET. Dashed lines in enlargements outline the nuclear envelope. (A and A′) CLEM overlay (A) with enlargement (A′) showing positions of IN.mScarlet signals (red; white arrow) at the nuclear envelope in an EM section post-stained with Hoechst (blue) and decorated with multi-fluorescent fiducials (Fd) for correlation. (A″) Slice through a tomographic reconstruction at the correlated position shown in (A) and (A′). The features i–iii that are shown enlarged in the bottom panel are framed in black and contain three different capsids that deeply penetrate the central channel of the NPC (green arrowheads). Cy, cytosol; Nu, nucleus; NE, nuclear envelope; NPC, nuclear pore complex. (A‴) Same as in (A″) but displayed segmented and isosurface rendered. MT (microtubule) red; capsid, magenta; NE, yellow; NPC, cyan (cryo-EM map of NPC: [23]). See also Video S2. (B – B″) Same as (A and A″) showing capsid docking at the NPC (i) and capsid located in the nuclear basket region (ii) from the same resin section. Both capsids display a conical shape and a dense interior (black arrowheads). (C) Slices through tomographic reconstructions from two different resin sections, showing two cone-shaped capsids located in the NPC basket region oriented with their narrow ends toward the NPC density. Both capsids display a dense interior. (C′) Same as in (C, inset i) but displayed segmented and isosurface rendered.

The cyclophilin A binding site is occupied on cytosolic capsids

To investigate the structure of the capsid and its interaction with nuclear pores in more detail, we used cryo electron tomography (cryo-ET). We subjected MDM infected with NNHIV for 48 h and control uninfected cells to specimen thinning by focused ion beam (FIB) milling and acquired 93 and 52 tilt series, respectively (Figure S2, Table S1). In the reconstructed tomograms, we identified 13 enveloped particles outside of cells and 36 capsids inside of cells, either in the cytosol, the nucleoplasm or associated with the NPC (Figure 4, see also Video S3); ten of these capsids were located in direct proximity or inside of nuclear pores (Figure 5A). The capsids appeared to be morphologically intact, and the large majority displayed interior density as typically observed for the nucleoprotein complex.

We used subtomogram averaging (STA) of capsid surfaces as previously described [15, 39] to structurally analyze the capsid lattice *in situ*. This analysis identified to a large extent the expected hexagonal signature of the CA lattice as well as CA pentamers inside virions, in the cytosol and also for capsids inside the central channel of the NPC (Figure 4B). The lattice was clearly detectable in nuclear capsids as well, but it appeared overall less complete (Figure 4B). Whether these local differences in the nucleoplasm are caused by reduced contrast due to molecular crowding, or alternatively by partial loss of capsid integrity cannot be judged at present.

We hypothesized that the CA lattice might be decorated by different binders during the infection process and categorized our subtomograms according to the subcellular localization of the capsid. As expected, the structure of the CA hexamer and pentamer in enveloped particles outside of cells was very similar to previously analyzed purified particles [15], (Figure 4C, D). Inside the cytosol, hexamers and pentamers were also clearly detected but their structure contained additional density consistent with published in vitro structures of CypA bound to CA [11,40], in both hexamers and pentamers (Figure 4C,D,E). The respective density was strongly reduced in subtomogram averages obtained from capsids inside the central NPC channel and in the nucleoplasm (Figure 4C), supporting a model in which CypA is bound to the majority of CA hexamers in the cytosol and stripped from the capsid upon NPC entry.
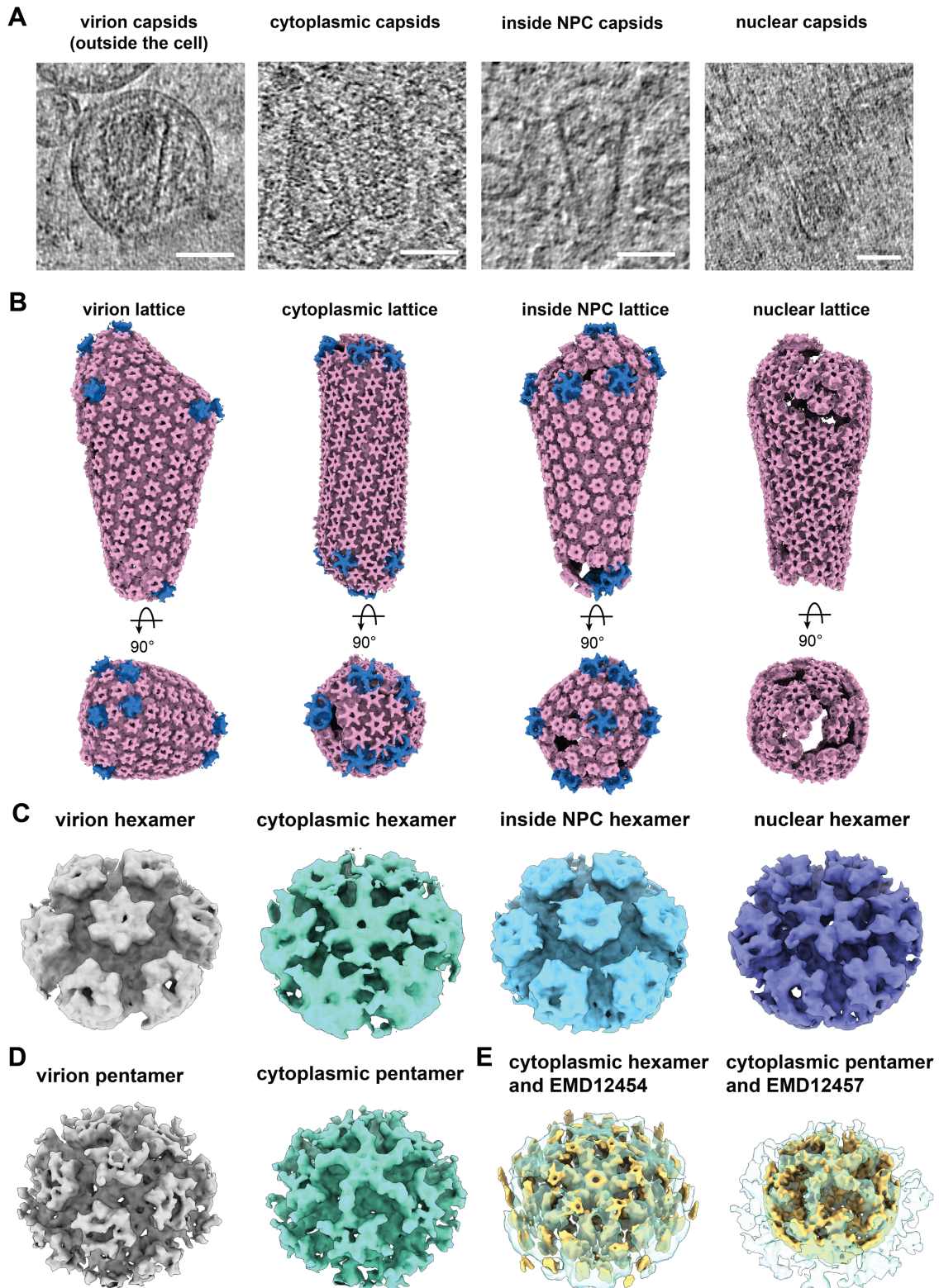
Figure 4. **CA lattice is detected in the cytoplasm, during and post nuclear entry.** (A) Exemplary virtual slices through cryo-tomograms of HIV-1 capsids inside virions, in the cytoplasm, inside NPCs and in the nucleus. (B) Hexameric capsid lattice traced by STA of CA hexamers in virions, the cytoplasm and inside the central channel and the nucleoplasm. Exemplifying capsids are displayed in side view and a top view looking at the wide end of the capsid. Respective subtomogram averages are shown in pink for the hexamers and in blue for the pentamers. The positions of pentamers were inferred from the hexagonal lattice, where

possible, and subsequently subjected to STA. For capsids inside of NPCs, the number of detectable pentamers was insufficient for independent STA. Instead pentamers were combined with those from cytoplasmic capsids. (C) STA of the HIV-1 CA hexamer for virion (grey), cytoplasmic (mint), inside NPC (light blue) and nuclear capsids (purple) shows additional density between the individual CA hexamers only for the cytoplasmic average. (D) STA of the HIV-1 CA pentamer for virion (grey) and cytoplasmic (mint), shows additional density between the central CA pentamer and its neighbors for the cytoplasmic average. (E) Published in vitro structures of CA hexamer and pentamer with CypA bound (EMD12454 and EMD12457 respectively [40], both yellow) are shown overlayed with the cytoplasmic capsid averages from this study (both mint). The additional density between neighboring subunits in the cytoplasmic capsids matches where CypA binds in the in vitro structure. Scale bar in (A): 50 nm.

The NPC scaffold in macrophages is wider than most capsids

Previous analysis in the SupT1 T-cell line by STA pointed to an overall dilated (64 nm at the IR) [23], but otherwise normal three-ringed NPC architecture both in infected and control cells, and the diameter of NPCs engaged with capsid was within the overall observed range [23]. However, the number of capsids observed inside of NPC by cryo-ET was small and these capsids contained the A77V mutation defective in CPSF6 binding. It has been argued that capsids may have to induce additional NPC widening in order to pass through the central channel [41]. To analyze NPC architecture and width of the central channel in MDM, we subjected 200 and 118 NPCs from infected and control cells, respectively, to STA. The resulting overall structure was reminiscent of previous analyses in Hek293 and SupT1 cells [23, 26] (Figure S3A, B). No obvious structural differences were apparent between NPCs from infected and control cells, nor was their NPC diameter significantly different at the IR (Figure S3B, C). However, NPCs in MDM were on average wider than in the previously analyzed SupT1 cells [23] (Figure S3B). The IR displayed a more variable diameter as compared to the CR and NR, consistent with the fact that the IR spokes are flexibly connected [26]. At the given inner diameter of the scaffold in macrophages (~65 nm, Figure S3D) the NPC would appear to be wide enough to accommodate most HIV-1 capsids with an average diameter of ~60 nm at their wide end (Figure S2F). To which extent the bulk of FG-Nups contributes to the effective diameter could not be estimated from this analysis however, because it emphasizes scaffold Nups, while FG-Nups are averaged out.

Nuclear pores crack upon passage of the HIV-1 capsid

Recent advances in template matching technology have allowed us to identify subunits of individual nuclear pores [42, 43]. To structurally analyze the scaffold of those NPCs that are engaged with a capsid, we used rotational segments of the CR, IR and NR for template matching, as previously described [43]. Visual inspection of the constrained cross-correlation (CCC) volumes revealed that five out of the ten NPCs engaged with capsid had a distorted scaffold, in which the subunit positioning was not entirely in agreement with the geometry of the canonical 8-fold rotational symmetry (Figure 5A, B). These distortions did not occur homogeneously distributed across the ring structure, but rather at a specific position where the interior angle of the polygon (IAOP) (cartoon in Figure 5C), i.e. the rotation around the symmetry axis from a given to the neighboring subunit, was increased. Concomitantly, this angle was compressed for remaining subunits, thus indicating a rupture event that had cracked the ring structure of the scaffold. Such NPC cracking events were not observed in the three cases where capsids were found associated with the cytosolic face of the NPC, but only in NPCs in which the capsid had penetrated considerably into the central channel. In two NPCs with a capsid deep in the central channel, template matching indicated 9 subunits of the IR (Figurer 5A, II and III, Figure S3E, Video S4). More frequently, however, ring cracking events co-occurred with apparent subunit losses. These were also observed in NPCs that showed a capsid associated with the nuclear face, indicative of damage induced during nuclear entry of this capsid.
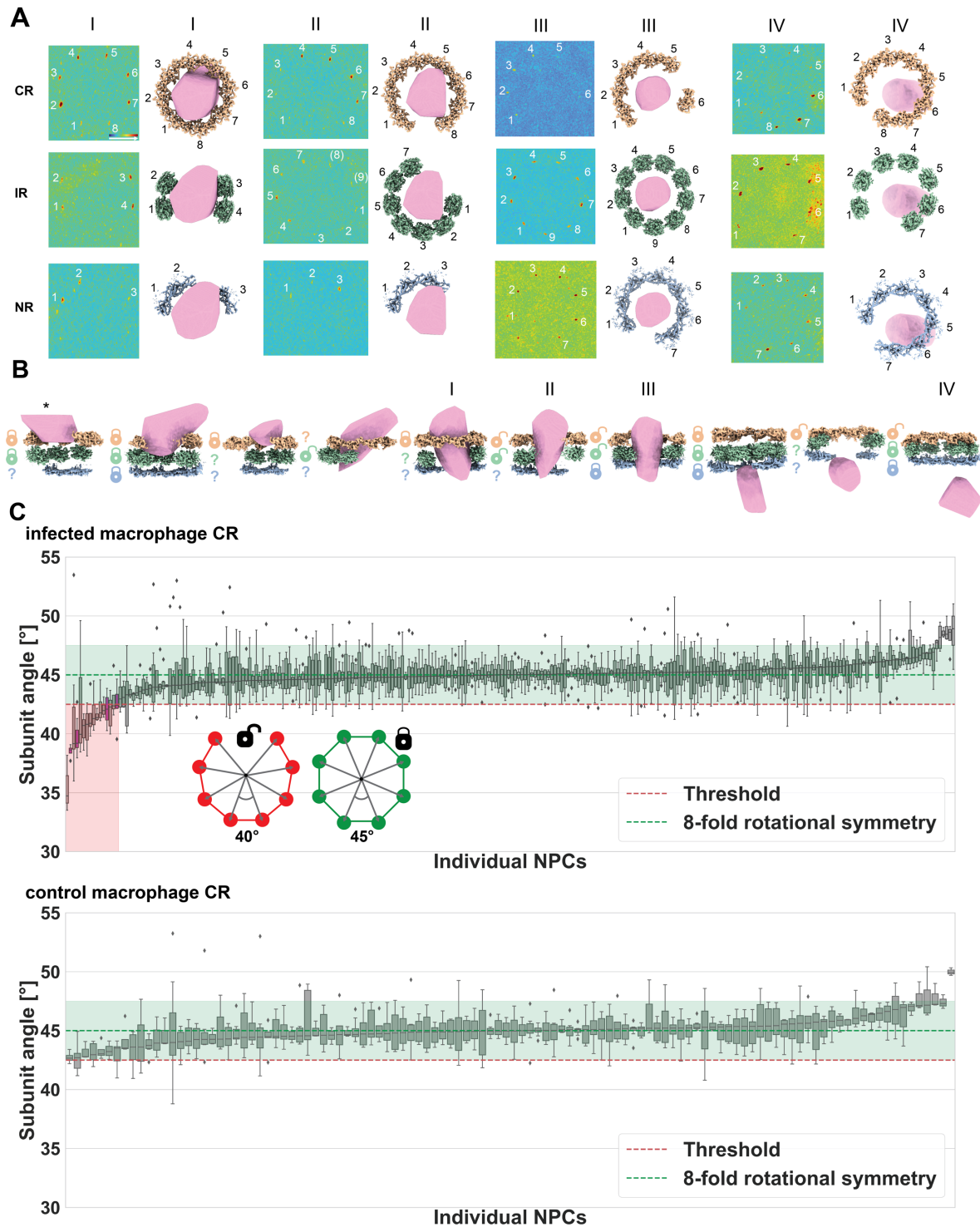
Figure 5. **The presence of HIV capsid inside the NPC is linked to abnormal NPC subunit arrangements.** (A) Template matching results for subunits of all three NPC rings (CR (light orange, top row), IR (green, middle row), NR (blue, bottom row) for four exemplary NPCs that are associated with an HIV capsid (surface rendering, pink). For each NPC a maximum intensity projection of the constrained cross-correlation (CCC) volume with peaks for that ring subunit is shown color-coded (low CCC values in blue and high values in red). The respective subunit arrangements are indicated in the right panels. (B) Cross section gallery of NPCs sorted according to capsid position. The locks next to each NPC ring represent the status of that ring as either being unperturbed (closed lock) or cracked, the latter meaning inconsistent with the

canonical 8-fold rotational symmetry (open lock). This assignment is based on the IAOP (see methods) and a threshold of 42.5°. The asterisk denotes a case where the capsid is only partially contained in the tomographic volume. Question marks represent cases where the number of detected subunits was insufficient for assignment (less than three angle measurements) into either category. For the infected MDM dataset, NPCs without associated capsid were C8-symmetric 247 times and had cracked CR rings twelve times. NPCs with associated capsid were significantly more often cracked (Fisher's exact test, p=0.0009; four out of nine cracked CR rings). (C) Comparison of the median IAOP per NPC for the CR of HIV-infected and control uninfected MDM. The angles for each CR are plotted as boxplots and sorted by median and are shown in the red transparent box if below a threshold of 42.5° (purple boxes had capsid associated). Angles consistent with C8-symmetric rings are shown in the green transparent box (42.5° - 47.5°). This signature was significantly more frequent in CRs of infected as compared to control MDMs (Fisher's exact test, p=0.0043; 252 C8-symmetric and 16 cracked rings in infected MDM and 112 C8-symmetric and zero cracked rings in control MDM).

NPC cracking is specific to infected macrophages

Nuclear entry of HIV-1 is a rare event and we wanted to carefully assess the above-described observations for statistical significance. We therefore turned to an objective metric to quantify the number of cracking events in each of the three rings of the NPC. We defined NPC ring cracking events based on the compression of the IAOP of the majority of subunits of a given NPC (Figure 5C, see above). Using this sensitive assay, we first asked whether NPCs in infected MDM that had an associated HIV-1 capsid were more likely to display ring cracking compared to NPCs not associated with a capsid from the same cells. This was clearly the case (Fisher's exact test, n=268, p=0.0009 for the CR, see legend of Figure 5 for values). We furthermore showed that cracking occurred more frequently in NPCs in infected as compared to control cells, regardless of whether a capsid was found close by the respective nuclear pore (Figure 5C) (Fisher's exact test, n=380, p=0.0043 for the CR, see legend of Figure 5 for values). At the chosen angular threshold, no cracking events of the CR were observed in non-infected cells (Figure 5C), and they were rare at the level of the IR and NR in these cells (Figure S4).

These observations support the notion that passage of HIV-1 capsids induces NPC cracking. An alternative hypothesis would be that exceptionally large capsids are trapped at NPCs and induce damage, while normal-sized capsids would progress faster into the nucleus and thus were invisible to our analysis. We therefore analyzed whether the size of capsids associated with nuclear pores exceeded that observed for enveloped particles outside of cells. This was not the case (Figure S2F). The notion that nuclear entry of capsids is a rate limiting step in MDM was further supported by our light microscopic and CLEM data presented above; these experiments identified a high number of capsids at different positions of nuclear pores,

421   including the nucleoplasmic side, and showed that these capsids were visually intact and of

422   similar size as observed for intra-virion capsids.

423

424   **HIV capsids clash with NPC scaffolds in molecular dynamics simulations**

425

426   As the capsid approaches the NPC, each CA hexamer can be bound by one of the ~6,000 FG-

427   repeats. However, the balance between the resulting force pulling the capsid into the central

428   channel and the counterforces from displacing the bulk FG-Nups and clashes with the NPC

429   scaffold remains unclear. Molecular dynamics (MD) simulations in combination with FRET

430   measurements of FG-Nups have recently shed light on their conformational dynamics *in situ*

431   [44]. Here, we adapted this simulation framework to analyze the steric requirements for nuclear

432   entry of HIV-1 capsids, the response of the FG-Nup network, and the associated forces.

433   We performed coarse-grained MD simulations to gain a detailed view on the passage of HIV-

434   1 capsids through intact, dilated, and cracked NPCs with and without FG-Nups. We first built

435   an atomic model of a cone-shaped HIV-1 capsid of typical size by completing its well-

436   resolved fullerene-like lattice of CA hexamers and pentamers (Figure S5A,B). We then built a

437   model of the dilated (in-cell) human NPC including FG-Nups (Figure 6A) as described

438   previously for the constricted conformation [26, 44]. The interaction of capsid and FG-Nups was

439   matched to experiments [17, 44] (Figure S5C-E). To model NPC cracking, we split the scaffold

440   and widened it (Figures 6A-C and S7A-C). To cover the NPC diameter increase seen in

441   MDM (Figures S3B), we constructed intact, dilated scaffolds (Figure S7D-F).

442   With these different NPC scaffold models, we identified the minimal steric requirements for

443   HIV-1 capsid passage. In MD simulations of NPCs lacking the FG-Nup network (Figure

444   S6G-L), we found that steric clashes prevent passage of the capsid through the intact in-cell

445   NPC scaffold [26]. Passage required either dilating the IR diameter further to about 70 nm

446   (Figure S6J), as seen in ~50% of MDM NPCs (Figure S3D), or cracking the NPC scaffold

447   (Figure S6K,L). The additional mass of FG-Nups is expected to amplify this effect.

448   Therefore, for a more realistic description of capsid passage, we included the FG-Nup

449   network with interactions matched to experiments. In our MD simulations, FG-Nups in intact

450   and cracked NPCs readily latched on to the HIV-1 capsid, effectively increasing the capsid

451   diameter (Figure 6A-C, see also Video S5). Force-driven simulations (Figure S6G-L) and free

452   energy profiles for capsid passage (Figures 6D and S7) confirmed that capsid passage is

453   possible in the cracked and dilated states with diameters ≥70 nm, but sterically blocked in the

454   ~58-nm wide in-cell NPC. However, favorable interactions with the FG-Nups resulted in

455   distinct free energy minima for the bound state (Figure 6D), and require further widening for

456   the release of capsid (see Figure S6J-L The favorable interactions with the FG-Nups caused

457   the immersed capsid to tilt sideways (Figure 6E). [23]

458   From the MD simulations and consistent with earlier modeling [41], we conclude that capsids

459   face two distinct and substantial energetic barriers to exit from the central channel into the

460   nucleus, one caused by repulsive steric interactions with the NPC and the other by the

461   attractive interactions of the capsid with FG-Nups. As found here, the steric barrier can be

462   relieved by NPC cracks, whereas the attractions could be broken either by capsid rupture and

463   release of the HIV-1 genetic material into the nucleus or, alternatively, by competitive binding

464   of additional factors such as Nup153 and CPSF6 to the CA lattice.

465

466
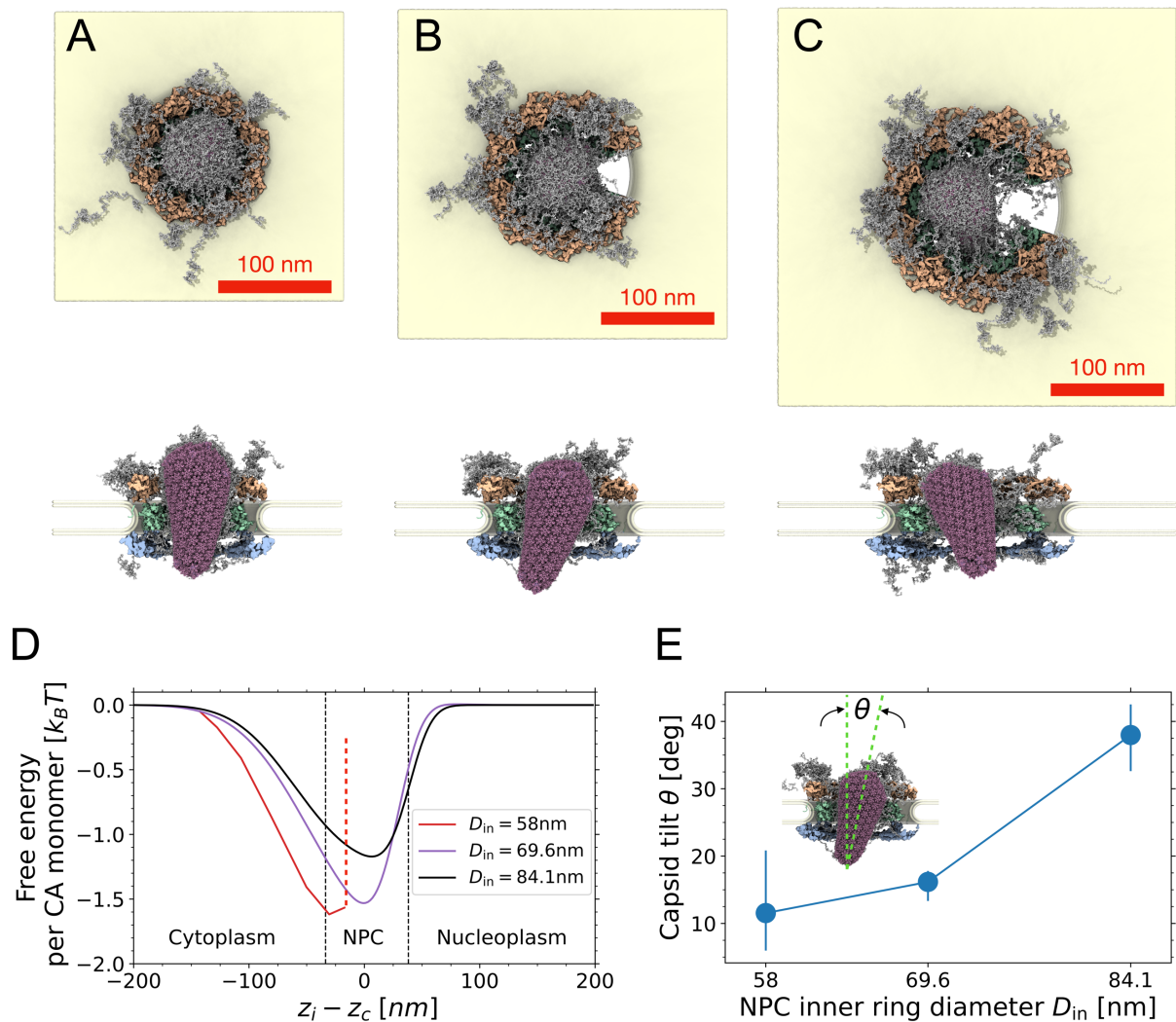
Figure 6. NPC cracking facilitates HIV capsid passage. (A-C) Snapshots of MD simulations of HIV capsid (violet) in intact NPC (A) with inner ring diameter $D_{in} = 58$ nm, and cracked NPCs with $D_{in} = 69.6$ nm (B) and $D_{in} = 84.1$ nm (C). Views from the cytosol (top) and the side (bottom) show end states of the simulations (FG-Nups: grey; CR: orange; IR: green; NR: blue; nuclear envelope: yellow). (D) Free energy profiles for HIV capsid passage through the NPC as a function of the vertical distance $z_C - z_i$ between the capsid center, half-way between its narrow and wide ends, and the inner ring (see Figures S7A-C for the capsid positions used to calculate the mean force shown in Figure S7D). Black dashed lines mark the extent of the NPC, and the vertical red dashed line indicates the position of the steric blockage of the HIV capsid inside the intact NPC. (E) Tilt angle (inset) of capsids released inside intact and cracked NPCs. Symbols and error bars indicate the average, minimum and maximum at the end of three replicas. The interaction strengths $\tilde{\epsilon}_{FG-FG} = 0.42$ and $\tilde{\epsilon}_{FG-CA} = 0.5$ between FG-Nups and CA hexamers and pentamers were matched to experiments. The snapshots were rendered using VMD [45].

Discussion

The data presented here allow us to assess the different scenarios for the nuclear entry of HIV-1 capsids introduced above. (i) By STA we did not identify deformation of the capsid lattice within the central channel of the NPC as compared to capsids localized elsewhere. (ii) We also did not observe breakage and morphological alteration of the capsid lattice inside the central channel. Instead, we obtained compelling evidence for scenario (iii): Passage of the HIV-1 capsid through the NPC channel of MDM alters the NPC scaffold. Our findings support a model (Figure 7) in which capsids decorated with CypA dock to the cytoplasmic face of the NPC, where CypA is stripped off, most likely by competitive interaction with the Cyp domain of Nup358 in the CR. The capsid is then drawn into the central channel by saturating the respective FG-binding sites towards the broad end of the capsid [31] As it penetrates more deeply, clashes with both the NPC scaffold and FG-Nups emerge. Entry into the limited space creates lateral force that in turn can lead to stretching of the NPC scaffold. NPC stretching may then extend the ring structure to a degree that it cracks, likely allowing a spatial re-distribution of FG-Nups and further progression of the capsid through the nuclear pore. We cannot exclude that capsid elasticity of scenario (i) could occur transiently and may thus contribute to nuclear entry of the capsid as well. Furthermore, potential capsid breakage as in (ii) could lead to complete capsid disintegration, thereby escaping detection. However, based on the high proportion of cracked pores and the observation of morphologically intact capsids in the nucleus, we propose that HIV-1 capsids pass the NPC more or less intact and, if sterically blocked, crack its rings.

503 We speculate that eventual capsid progression towards the nucleoplasm may be driven by

504 interactions with Nup153 FG-repeats. At the nuclear basket, the capsid may transiently remain

505 latched to the very long Nup153 FG-repeats and thus rotate in the chromatin-free region, as

506 occasionally observed in the simulations. This would agree with in vitro measurements of

507 binding constants of different FG-Nups [17, 46], and can explain both the observed delayed release

508 into the nucleoplasm and the variable orientation of nuclear basket associated capsids.

509 Ultimately, FG binding sites in the capsid lattice will be competitively saturated by abundant

510 nuclear CPSF6, causing capsid release from the nuclear basket to migrate deeper into the

511 nucleoplasm. This model is consistent with CPSF6 gene silencing experiments and mutation

512 of the CPSF6 binding site in CA; in these cases, capsids were prominently observed close to

513 the nuclear basket region and differences in HIV-1 integration sites were found [20, 23].
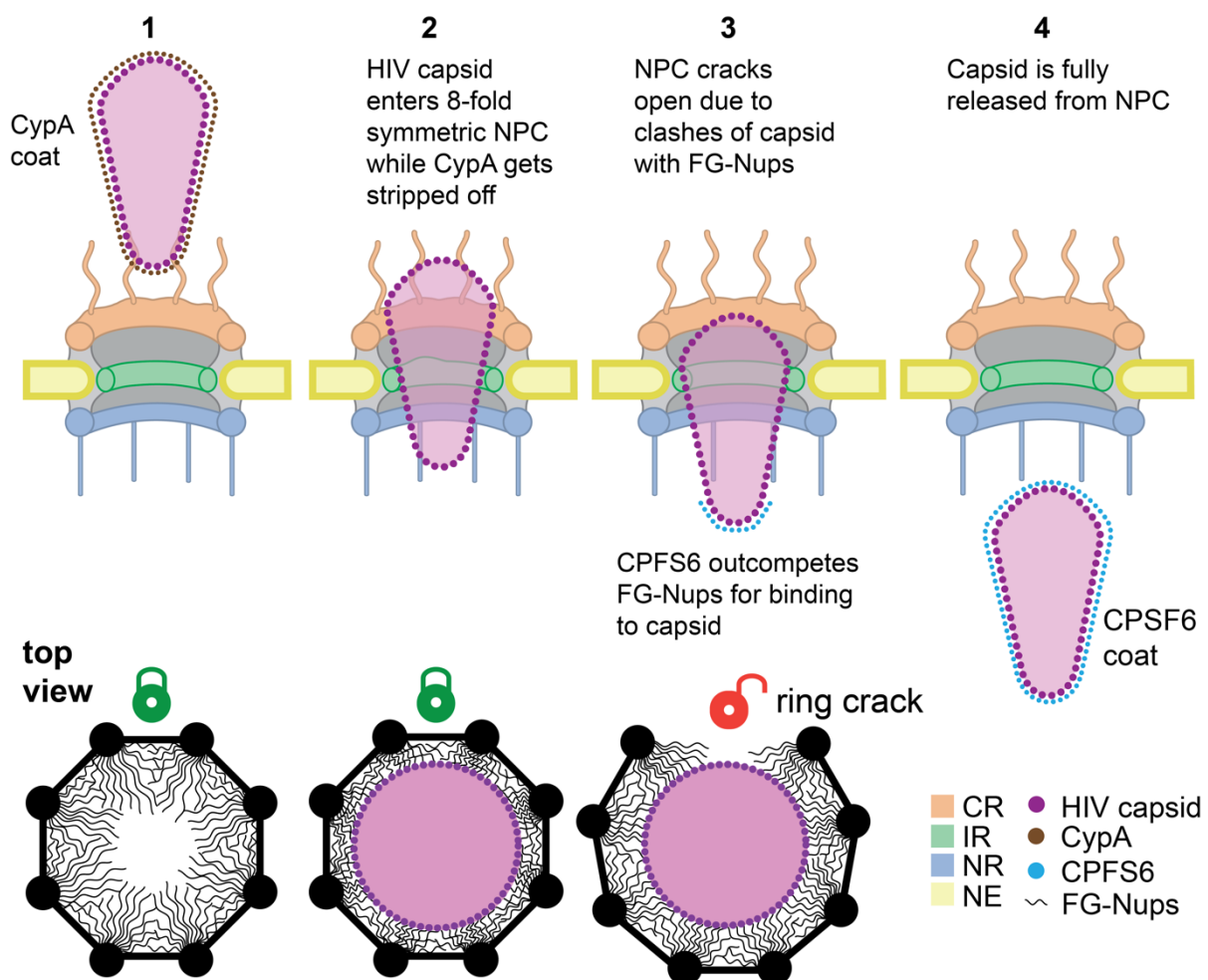
514

515 **Figure 7. Model for nuclear entry of the HIV-1 capsid in macrophages.**

516 (1) Side view cross section: A cone-shaped HIV-1 capsid decorated with CypA is oriented
517 with its narrow end towards the cytoplasmic face of the NPC. The cytoplasmic filaments of
518 the CR guide and orient the capsid for further entry into the pore. The top view cross section
519 below shows the intact (green closed lock) C8-symmetric ring structure with the FG-Nups

520 extending into the central channel. (2) Side view cross section: The cone-shaped capsid is
521 partially inserted into the central channel of the NPC, thereby losing the associated CypA. Its
522 wide end has not yet passed through the narrowest point of the NPC scaffold (CR opening).
523 The top view shows the intact (green closed lock) C8-symmetric ring structure with the
524 capsid inserted. The FG-Nup mesh network is compressed due to the capsid insertion. (3)
525 Side view cross section: The capsid has passed through the CR opening by cracking the NPC
526 scaffold and is now fully inserted into the widened central channel of the NPC. CPFS6 starts
527 to coat the tip of the capsid as it reaches the nucleoplasm by outcompeting FG-Nups. The top
528 view shows the cracked (red open lock) ring structure with the capsid inserted. The FG-Nup
529 mesh network relaxes due to the ring crack. (4) Side view cross section: The capsid has been
530 released from the nucleoplasmic side of the NPC and has acquired a full CPFS6 coat. The
531 HIV-1 capsid, CPFS6 and the individual rings and FG-Nups of the NPC are shown color-
532 coded.
533

534 We had previously found that cone-shaped capsids enter dilated NPCs in T-cells [23]. However,

535 cryo-ET had captured only few events, and thesecapsids contained the A77V mutation

536 defective in CPSF6 binding. Moreover, by analyzing the NPC architecture through

537 subtomogram averaging, differences across a small set of individual particles could not be

538 readily detected. Here, by using template matching of NPC subunits [42,43] we could reliably

539 detect damage of individual NPCs and, by greatly expanding the statistics, connect NPC

540 cracking to HIV capsid passage.

541 That the HIV-1 capsid cracks the NPC was not necessarily intuitive, because the NPC scaffold

542 is an elaborate structure designed to persist strain laterally imposed by the nuclear membranes

543 [25,43,47], while the capsid has to disintegrate at some stage during the post-entry process. The

544 exact forces remain challenging to measure experimentally. In the MD simulations, forces of

545 10-100 pN pull the capsid into the NPC central channel (Figure S7D), which is in the range of

546 forces required for sub-second unfolding of proteins [48]. The cone shape of stuck capsids

547 converts this axial force into a radial force that could drive NPC cracking. Instead of the NPC

548 cracking the capsid, the capsid cracks the NPC.

549 Deviations from the canonical 8-fold rotational symmetry of the NPC occur only rarely under

550 native conditions [49]. A recent study investigating NPC subunit arrangement and diameter

551 during stem cell differentiation has detected abnormal rotational symmetries and NPC

552 overstretching as a result of knock out of the scaffolding Nup133 [43]. In contrast to this study,

553 however, straining of the NPC scaffold by the HIV-1 capsid occurs from the inside. The

554 observed distortions are markedly different, indicating that the changes observed by Taniguchi

555 et al. are of different origin. Specifically, Taniguchi et al. did not observe rotational symmetry

556   mismatches across the three rings within individual NPCs, but rather NPCs were overstretched
557   and disintegrated, thereby detaching from the nuclear membranes [43]. Ring cracking by HIV-1
558   capsid passage shows specific features: subsequent to cracking of one ring, the scaffold
559   contacts with the next ring do not rotationally register. This finding is intriguing because it
560   emphasizes that the NR and CR have intrinsic stability. Furthermore, our results show that
561   nuclear pores may transport cargos that are larger than their diameter.

562   The findings presented here provide an explanation for the evolution of the unique HIV-1
563   capsid structure. Protecting the genome and allowing reverse transcription inside a protective
564   shell requires a closed structure, but not this cone-shaped geometry. However, the complete
565   capsid also acts as the importin for nuclear entry of the HIV-1 subviral complex [32, 33], and this
566   is absolutely essential for infection of target cells that do not break down their nuclear envelope
567   during mitosis. Shape most likely reflects this function: the narrow end facilitates threading
568   into the narrow channel of the NPC, and the increasing width of the cone allows to
569   accommodate the volume requirement for the genome and provides avidity effects by an
570   increasing number of FG binding sites on the capsid lattice as it progresses into the NPC.
571   Maximum width may then be a trade-off between what is absolutely needed to package the
572   genome (most likely together with partial cDNA due to cytoplasmic reverse transcription) and
573   the size limit to pass through the (partly disintegrated) central NPC channel. Thereby, NPC
574   cracking might be a simple byproduct of HIV-1 nuclear entry with optimal payload, without
575   any direct consequences for infectivity. Importantly, damage to individual NPCs must be
576   compatible with cell viability as infected macrophages can survive for prolonged time. Could
577   there be a further benefit from NPC cracking for the virus? One may speculate that the capsid
578   lattice becomes mechanically prepared for rupture while it sheers at the NPC scaffold, but does
579   not immediately disintegrate because of rapid surface coating with CPSF6 upon reaching the
580   nuclear side. Whether this is the case, and whether there may be other benefits for the virus,
581   e.g. inducing nuclear envelope rupture and thus locally changing the nuclear proteome, remains
582   to be further investigated.

Materials and Methods

Cells

Human embryonic kidney 293T cells (HEK293T) [50] were maintained in Dulbecco's modified Eagle medium (DMEM; Thermo Fisher Scientific) supplemented with 10% fetal bovine serum (FBS; Capricorn Scientific GmbH, Germany), 100 U/ml penicillin and 100 mg/ml streptomycin (Thermo Fisher Scientific). Monocyte-derived macrophages (MDM) were obtained from human peripheral blood mononuclear cells (PBMC) isolated from buffy coats of healthy donors as described previously [20]. Buffy coats were obtained from anonymous blood donors at the Heidelberg University Hospital Blood Bank according to the regulations of the local ethics committee. MDM were cultivated in RPMI 1640 medium (Thermo Fisher Scientific) supplemented with 10% heat inactivated FBS, antibiotics (as above), and 5% human AB serum (Capricorn Scientific GmbH, Germany). Cells were cultivated at 37ºC in a humidified incubator with a 5% CO_2 atmosphere. For seeding, MDM were detached by Accutase (StemCell Technologies) according to the manufacturer's instructions.

Plasmids

Plasmid pNNHIV for production of non-infectious, reverse transcription competent HIV-1 particles [23], the proviral plasmids pNL4-3 [51] and pNL4-3ΔEnv [20], and the Vpr.IN$_{D64N/D116N}$.mScarlet fusion protein encoding plasmid pVpr.IN$_{D64N/D116N}$.mScarlet [23] were described previously. Plasmid pEnv-4059 encoding an R5-tropic Env from a clinical HIV-1 isolate [52], was kindly provided by R. Swanstrom (University of North Carolina, Chapel Hill, NC, USA). Plasmid pVpr.IN.eGFP encoding a Vpr.IN.eGFP fusion protein with an HIV-1 protease recognition site between Vpr and IN [53], was kindly provided by A. Cereseto (CIBIO, Mattareo, Italy). Plasmid pNNHIVΔEnv contains a 1 bp fill-in of an StuI site in the *env* ORF resulting in a frameshift and premature stop codon (primers used for PCR: forward, 5'-CAGACAGGCCTCGTCCAAAGGTATCCTTTGAG-3'; reverse, 5'-CAGACGCTAGCTATCTGTTTTAAAGTGGCATTC-3').

Antibodies

For immunofluorescence staining, rabbit polyclonal antiserum against HIV-1 CA raised against purified recombinant protein (in house) [54], mouse monoclonal antibody against human lamin A/C (sc-7292; Santa Cruz), mouse monoclonal antibody against Nup153 (ab24700; Abcam) and mouse monoclonal antibody against FG-Nups (Mab414) (ab24609; Abcam) were used at a dilution of 1:1,000, 1:100 and 1:200, respectively. For spinning disc confocal microscopy, secondary antibodies donkey anti-rabbit IgG and donkey anti-mouse IgG conjugated with Alexa Fluor 488 and 647 (Thermo Fisher Scientific), respectively, were used at 1:1,000 dilution. For STED microscopy, secondary antibodies goat anti-rabbit IgG and goat anti-mouse IgG conjugated with Atto 594 (Merck; 77671) and Abberior® STAR RED (Merck; 52283), respectively, were used at 1:200 dilution.

Virus and virus-like particles

HIV-1 virions and non-infectious virus-like particles were produced in HEK293T cells grown on 175 cm^2 tissue culture flasks (side bottom) transfected with respective plasmids (total 70 µg DNA per flask) using calcium phosphate transfection. For production of infectious R5-tropic HIV-1, cells were transfected with pNL4-3ΔEnv and pEnv-4059 at a molar ratio of 4.5:1. To produce IN.eGFP labeled R5-tropic HIV-1, cells were transfected with pNL4-3ΔEnv, pVpr.IN.eGFP and pEnv-4059 at a molar ratio of 4.5:1:1. For production of non-infectious IN.mScarlet labeled R5-tropic NNHIV, cells were transfected with pNNHIVΔEnv, pVpr.IN$_{NN}$.mScarlet and pEnv-4059 at a molar ratio of 4.5:1:1. Medium was changed 6 h after transfection and cells were further incubated at 37ºC and 5% CO2. At 44 h post-transfection, culture media from virus-producing cells were harvested and cleared by filtration through a 0.45 µm nitrocellulose filter (Carl Roth, Germany), and particles from media were concentrated by ultracentrifugation through a 20% (w/w) sucrose cushion for 90 min at 27,000 rpm (at 4ºC) in a Beckman SW32 rotor (Beckman Coulter Life Sciences). Particles were resuspended either in PBS or in PBS containing 10% FBS and 10 mM HEPES (pH 7.2), then aliquoted and stored at –80ºC. Particle-associated RT activity was determined by SYBR Green-based Product-Enhanced Reverse Transcription assay (SG-PERT) [55].

Sample preparation for confocal and STED microscopy

MDM seeded in 8-well μ-Slides with a glass bottom (ibidi GmbH, Germany) were infected with non-labeled or fluorescently labeled wild-type HIV-1 or NNHIV (5–15 μUnits of RT/cell) pseudotyped with R5-tropic 4059 Env and incubated at 37°C until indicated time post-infection. For both spinning disc confocal and super-resolution STED microscopy, samples were fixed with 4% FA in PBS (15 min), rinsed with PBS, permeabilized with 0.5% Triton X-100 in PBS (5–20 min) and washed three times (5–10 min) with PBS. For detection of nuclear HIV-1 CA, cells were further extracted using ice-cold methanol for 10 min (at –20ºC) and subsequently washed twice with 3% bovine serum albumin (BSA) in PBS. Samples were blocked with 3% BSA in PBS for 30 min and staining with primary and secondary antibodies (both diluted in 0.5% BSA in PBS) was carried out at room temperature for 1 h each. When relevant, cell nuclei were visualized by DNA staining with 0.2 μg/ml Hoechst33258 (Thermo Fisher Scientific) in PBS for 30 min.

Spinning disc confocal microscopy

Spinning disc confocal microscopy (SDCM) was performed using a Nikon Ti Perkin Elmer Ultra VIEW VoX 3D spinning disk confocal microscope (Perkin Elmer, MA, USA) equipped with a 100× oil immersion objective (NA 1.4; Nikon). Multichannel z series of randomly selected cells were acquired with a z-spacing of 200 nm and excitation with the 405-, 488-, 561-, and 640-nm laser lines, using the Volocity software (Perkin Elmer, MA, USA).

STED microscopy

Stimulated emission depletion (STED) imaging was performed with a 775 nm Expert Line STED system (Abberior Instruments GmbH, Germany) equipped with an SLM-based easy3D module and an Olympus IX83 microscope using a 100× oil immersion objective (NA 1.4; Olympus UPlanSApo). Dual-color STED images were acquired line sequentially, using the 590- and 640-nm excitation laser lines and two APD spectral detectors set to collect photons with the wavelength between 590–630 nm and 650–720 nm, respectively. Acquisitions using 405- and 488-nm laser lines were in confocal mode only. Nominal STED laser power was set to 15–40% of the maximal power of 3 W with 10 μs pixel dwell time, 15 nm pixel size and 9× accumulation. Acquired STED images were deconvoluted with Huygens Deconvolution software (Scientific Volume Imaging) using Classic Maximum Likelihood Estimation (CMLE)

671 algorithm and Deconvolution Express mode with 'Conservative' settings. For 3D STED data

672 acquisition, 30% of the STED laser power was used for fluorescence depletion in the Z-axis

673 and RESCue illumination scheme was used to minimize bleaching. Sampling frequency was

674 20 nm in xy axis and 70 nm in z. For sampling of the entire nuclear volume (~6–10 μm along

675 the optical axis) by 3D STED, 80–150 super-resolved images were acquired. The bleaching

676 during the acquisition was reduced by implementing a light dose management (DyMIN) that

677 specifically activates and modulates the intensity of the STED depletion laser beam to switch

678 off fluorophores only near the fluorescent feature to be recorded [56].

679

680 *Image analysis*

681 Quantification of CA signals localized at the nuclear envelope or inside the nucleus of infected

682 MDM visualized by SDCM was performed using the Icy software ([57]). The volumes of

683 individual HIV-1 CA signals in acquired z-stacks were automatically detected using the spot

684 detector function. Objects displaying positive signal in the laminA/C or Hoechst channel were

685 classified as nuclear envelope (NE) associated or as intranuclear, respectively. Nuclear signals

686 were further visually examined and manually currated to ensure that objects located in nuclear

687 regions with very low or undetectable Hoechst staining were not excluded from the analysis.

688 To determine percentage of CA signals colocalizing with FG-Nups at the nuclear perihery in

689 infected MDM visualized by 3D STED, deconvoluted z-stacks were reconstructed using the

690 Imaris software (Bitplane AG, Switzerland). Individual HIV-1 CA signals were automatically

691 detected using the spot detector Imaris module, creating for each distinct fluorescent signal a

692 3D ellipsoid object with Z axis = 1.5*X,Y axis. For all objects in the proximity of NE, the

693 median signal intensity within objects was quantified for the FG-Nups channel. All objects

694 representing CA signals that had maximum FG-Nups signal intensity higher than 50 (a.u.) were

695 scored as co-localizing. The same threshold was applied to all four datasets. To quantify the

696 total amounts of nuclear pores per nucleus, individual FG-Nups signals were automatically

697 detected by spot detector module as above and counted. To estimate the NPC density, the

698 dimensions of nuclei mid-sections was measured using the Fiji software [58] and the surface area

699 of each nucleus was then calculated as the surface of ellipsoid.

Sample preparation for CLEM

4×10^4 MDM were seeded on carbon-coated sapphire discs (Engineering Office M. Wohlwend, Switzerland) placed in a glass-bottomed 'microwell' of 35 mm MatTek dish (MatTek, Ashland, MA, USA) and cultured for 16–24 h at 37ºC. Cells were infected with IN.mScarlet labeled NNHIV particles pseudotyped with R5-tropic 4059 Env at 60 µU RT/cell. At 48 h p.i., infected cells were cryo-immobilized by high pressure freezing using a HPM010 high pressure freezer (BAL-TEC, Balzers, Liechtenstein) and discs with frozen cells were transferred to freeze-substitution medium (0.1% uranyl acetate, 2.3% methanol and 1% H_2O in Acetone) at –90ºC. Subsequent freeze-substitution and embedding of samples in Lowicryl HM20 resin (Polysciences, Inc., USA) was performed in an EM AFS2 freeze-substitution device (Leica Microsystems) equipped with a EM FSP robotic solution handler (Leica Microsystems) according to Kukulski et al. ([59]), modified as follows: Samples were incubated in FS medium for 5 h at –90ºC and temperature was then raised to –45ºC (at 7.5ºC/h). Samples were washed with acetone (3 × 25 min) and infiltrated with increasing concentrations of Lowicryl HM20 in acetone (25, 50% and 75%; 3 h each), while raising temperature to –25ºC (3.3ºC/h). The acetone-resin mixture was replaced by pure Lowicryl HM20 for 1 h and the resin was exchanged three times (3, 5 and 12 h). Samples were polymerized under UV light for 24 h at –25ºC and polymerization continued for an additional 24 h while the temperature was raised to 20ºC (at 3.7ºC/h).

CLEM and electron tomography

250-nm thick resin sections were obtained using a EM UC7 ulramicrotome (Leica Microsystems) and placed on a slot (1 × 2 mm) EM copper grids covered with a formvar film (Electron Microscopy Sciences, FF2010-Cu). Grids were placed (section face-down) for 10 min on 20 µL drops of 1 × PHEM buffer (pH 6.9) containing 0.1 µm TetraSpeck beads (1:25) (Thermo Fisher Scientific) serving as fiducial markers and 10 µg/ml Hoechst33258 (Thermo Fisher Scientific) to stain nuclear regions in cell sections. Unbound fiducials were washed off on several drops of water and grids were transferred on 25 mm glass coverslips mounted in a water-filled ring holder for microscopy (Attofluor cell chamber, Thermo Fisher Scientific). Z stacks of sections were acquired with a PerkinElmer UltraVIEW VoX 3D spinning-disc confocal microscope (Perkin Elmer, MA, USA) and then visually examined using the Fiji software [58] to identify regions of interest (ROIs). Sections on EM grids were

732   stained with 3% uranyl acetate (in 70% methanol) and lead citrate. Individual grids were placed

733   in a high-tilt holder (Fischione Model 2040) and loaded to a Tecnai TF20 electron microscope

734   (FEI) operated at 200 kV, equipped with a field emission gun and a 4K-by-4K pixel Eagle CCD

735   camera (FEI). To map all cell sections on grid, a full grid map was acquired using the SerialEM

736   software [60]. To identify ROIs in resin cell sections for image acquisitions, EM images and

737   imported SDCM images were pre-correlated in SerialEM using the fiducials as landmark points

738   [61] and single-axis tilt series were acquired in correlated positions using SerialEM with a tilt

739   range from –60° to +60°, angular increment of 1° and a nominal pixel size of 1.13 nm.

740   Alignments and 3D reconstructions of tomograms were done with IMOD software [62]. High

741   precision post-correlation was performed using eC-CLEM plugin [63] in Icy software [57].

742

743   *Quantitative image analysis of capsids acquired by CLEM-ET*

744   Segmentation, isosurface rendering and quantitative analysis of the capsid interior were done

745   in the Amira software (Thermo Fisher Scientific) as described in Zila et al. [23]. Briefly, to

746   exclude the CA layer density from the interior of manually segmented capsid, the 'erosion'

747   algorithm was used to shrink the volume of segmented structure. The interior voxel intensity

748   median in shrunken volume was then determined using the 'label analysis' function and

749   normalized to intensity median of 3–5 volumes placed in the proximity of the structure. Only

750   structures fully covered in the EM section (not truncated at the section edge) were included in

751   the analysis.

752

753   *MDM vitrification and cryo-FIB milling*

754   MDM were detached by accutase (StemCell Technologies) according to the manufacturer's

755   instructions. 4×10^4 MDM were seeded on glow discharged and UV-light sterilized 200-mesh

756   EM gold grids coated with R 2/2 holey carbon films (Quantifoil Micro Tool GmbH), which

757   were placed in a glass-bottomed 'microwell' of 35-mm MatTek dish (MatTek, Ashland, MA,

758   USA). After seeding, cells were cultured for an additional 24 h at 37 ºC. For infection, cells

759   were incubated with IN.mScarlet labeled NNHIV particles pseudotyped with R5-tropic 4059

760   Env at 60 µU RT/cell for 48 hours. Mock-infected and infected MDM were vitrified by plunge

761   freezing into liquid ethane at –183°C using an EM GP2 plunger (Leica Microsystems). The

762   blotting chamber was maintained at 37°C temperature and 90% humidity. Before plunge

763   freezing, 3 µl of culture medium were applied onto grids. Subsequently, the grids were blotted

764 from the back side for 3 s with a Whatman filter paper, Grade 1, and plunge frozen. The samples

765 were then cryo-FIB milled using an Aquilos 2 microscope (Thermo Fisher Scientific) similar

766 to a previously described workflow [64]. In brief, samples were coated with an organometallic

767 platinum layer using a gas injection system for 10 sec and additionally sputter coated with

768 platinum at 1 kV and 10 mA current for 10 sec. Milling was performed with AutoTEM (version

769 2.4.2) (Thermo Fisher Scientific) in a stepwise manner with an ion beam of 30 kV while

770 reducing the current from 1000 pA to 50 pA. Final polishing was performed with 30 pA current

771 with a lamellae target thickness of 200 nm.

772

773 *MDM cryo-ET data acquisition*

774 Cryo-ET data for infected and control macrophages were collected at 300 kV on a Titan Krios

775 G4 microscope (Thermo Fisher Scientific) equipped with a E-CFEG, Falcon 4 direct electron

776 detector (Thermo Fisher Scientific) operated in counting mode and Selectris X imaging filter

777 (Thermo Fisher Scientific). For each grid, montaged grid overviews were acquired with 205

778 nm pixel size. Montages of individual lamellae were taken with 30 nm pixel size. Tilt series

779 were acquired using SerialEM (version 4.0.20) [60] in low dose mode as 4K x 4K movies of 10

780 frames each and on-the-fly motion-corrected in SerialEM. The magnification for projection

781 images of 53000x corresponded to a nominal pixel size of 2.414 Å. Tilt series acquisition

782 started from the lamella pretilt of $\pm$ 8° and a dose-symmetric acquisition scheme [65] with 2°

783 increments grouped by 2 was applied, resulting in 61 projections per tilt series with a constant

784 exposure time and targeted total dose of ~135 e$^-$ per Å^2. The energy slit width was set to 10 eV

785 and the nominal defocus was varied between -2.0 to -4.0 μm. Dose rate on the detector was

786 targeted to be ~4-6 e$^-$ /px/sec.

787

788 *Tomogram reconstruction*

789 The motion corrected tilt series were corrected for dose exposure as previously described [66]

790 using a Matlab implementation that was adapted for tomographic tilt series [67]. Projection

791 images with poor quality were removed after visual inspection. The dose-filtered tilt series

792 were then aligned with patch-tracking in AreTomo (version 1.33) [68] and reconstructed as back-

793 projected tomograms with SIRT-like filtering of 15 iterations at a binned pixel size of 9.656 Å

794 (bin4) in IMOD (version 4.11.5) [62] From the reconstructed tomograms, those containing

795 nuclear pore complexes and/or HIV capsids were selected by visual inspection.

796   The same tomograms were also reconstructed with 3D-CTF correction using novaCTF [69] with

797   phase-flip correction, astigmatism correction and 30 nm slab. Tomograms were binned 2x, 4x

798   and 8x using Fourier3D [B. Turoňová, turonova/Fourier3D: Fourier3D, Version v1.0, Zenodo

799   (2020)].

800

801   *HIV CA hexamer subtomogram averaging*

802   Capsid-like structures were identified in the infected macrophage SIRT-like filtered bin4

803   tomograms and then manually segmented in napari [napari contributors (2019). napari: a

804   multi-dimensional image viewer for python. doi:10.5281/zenodo.3555620]. The

805   segmentation was used to create a convex hull with the cryoCAT package. Subtomogram

806   averaging of the capsid hexamer was performed similarly to a previously described protocol

807   [15]. In detail, first the segmented capsid surfaces (at 4x binning) were oversampled with a

808   sampling distance of 2 voxels and each position was assigned an initial orientation that was

809   determined based on the normal vector of the segmented cone surface at given position (the

810   in-plane angle was assigned randomly). Then the coordinates were multiplied by factor of 2

811   to obtain positions for bin2 tomograms. All subsequent subtomogram alignment and

812   averaging was performed with imposed C6 symmetry in novaSTA [Turoňová, B.

813   turonova/novaSTA: Advanced particle analysis, Version v1.1. Zenodo (2022)].

814   For virion capsids, the oversampled positions of four capsids were used to extract bin2

815   subtomograms from 3D-CTF corrected tomograms. These subtomograms were used to

816   generate an initial featureless average and then aligned for six iterations. A distance threshold

817   of 16 voxels was used to remove overlapping subtomograms (i.e. particle duplicates). Low

818   CCC threshold and/or incorrect orientation (both assessed visually in using ArtiaX [70] lead to

819   additional removal of subtomograms. The resulting subtomograms were then aligned for six

820   iterations to obtain a better average and lattice arrangement. After further removal of

821   suboptimal positions, the final subtomograms were again aligned for six iterations.

822   This STA map of the virion hexamer was then used as an existing reference (lowpass filtered

823   to 40 Å) to align all oversampled virion capsid positions and obtain more complete lattices.

824   The resulting positions were used to remove duplicates and suboptimal positions as described

825   above. After multiple iterations of removal of incorrectly oriented positions and then manual

826   addition of potential positions to complete the lattice again in ArtiaX [70], the final

827   subtomograms were again aligned for nine iterations (for final particle numbers see Table S1)

828   For capsids in the cytoplasm, inside NPCs or in the nucleus, the same procedure was applied.

829

HIV CA pentamer subtomogram averaging

831   All subsequent subtomogram alignment and averaging was performed with imposed C5

832   symmetry in novaSTA [Turoňová, B. turonova/novaSTA: Advanced particle analysis, Version

833   v1.1. Zenodo (2022)]. Positions and orientations for subtomogram averaging of the CA

834   pentamer were obtained by placing particles into the areas of the capsid lattice where

835   hexamers were arranged around a pentamer hole as visualized in ArtiaX [70]. Virion candidate

836   positions were processed separately from cytoplasmic and inside NPC candidate positions. In

837   each case, the candidate positions were used to extract bin2 subtomograms from 3D-CTF

838   corrected tomograms. These subtomograms were used to generate an initial featureless

839   average and then aligned for nine iterations. Low CCC threshold and/or incorrect orientation

840   (both assessed visually in using ArtiaX [70] } led to additional removal of subtomograms. The

841   final subtomograms were aligned for nine iterations (for final particle numbers see Table S1).

842   For FSC calculations, the virion pentamer was treated as halfmap1 and EMD-3466 [15] as

843   halfmap2 and the resolution evaluated at FSC=0.5. The cytoplasmic pentamer map was

844   treated as halfmap1 and EMD-12457 [40] as halfmap2 and the resolution evaluated at FSC=0.5.

HIV CA pentamer template matching

846   A published CA pentamer STA map (EMD-3466 [15]) was downsampled to a pixel size of

847   4.828 Å (bin2 for this dataset) and then used as a search template to perform template

848   matching in parts of a bin2 tomogram with capsid-like structures using GAPSTOP^{TM}

849   [https://gitlab.mpcdf.mpg.de/bturo/gapstop_tm] [42]. The angular search range was set to 5-

850   degree angular sampling. The highest CCC peaks from template matching were extracted

851   with their corresponding orientations and then visually inspected in ArtiaX [70] to obtain only

852   the plausible candidates that are oriented correctly to the capsid surface as visible in the

853   tomogram.

NPC particle selection and subtomogram averaging

855   Positions of NPCs were manually selected in the bin4 SIRT-like filtered tomograms as

856   described previously [71]. Extraction of particles from the novaCTF-corrected tomograms,

857 subtomogram alignment and averaging was performed using novaSTA [Turoňová, B.

858 turonova/novaSTA: Advanced particle analysis, Version v1.1. Zenodo (2022)]. NPC

859 averaging was performed as described previously [25]. First, an average of the whole NPC was

860 obtained while utilizing C8 symmetry and a cylindrical mask. Next, coordinates of the

861 subunits were extracted based on the aligned positions using C8 symmetry. With these

862 subunit positions an average structure of the asymmetric unit of the NPC was obtained using

863 an elliptical mask. To obtain averages of individual NPC rings, first particle positions were

864 re-centered to the respective area (CR, IR, NR, LR, nuclear basket) based on their position in

865 the subunit average. Then the newly extracted bin4 subtomograms for the individual rings

866 were aligned and averaged with elliptical masks. To generate C8 symmetric composite NPC

867 maps, first the final averages of individual ring maps were fitted into the asymmetric subunit

868 average. Then the composite map was created by applying symmetry based on the

869 coordinates used for splitting the initial whole NPC average into asymmetric units. The entire

870 NPC STA procedure was first performed for control and infected macrophage NPCs

871 separately and then redone for the combined set of NPCs after determining no discernible

872 difference between the two macrophage NPC structures (control and infected).

873

874 *NPC diameter measurements*

875 The NPC diameters at different points were measured based on the coordinates obtained from

876 STA maps of individual rings (CR, IR, NR) using previously published MATLAB scripts [25].

877 Using ChimeraX [72], the measurement point of interest coordinates in the individual ring

878 average were determined with the marker tool and the particle list coordinates were offset by

879 the shift between the center of the average and the measurement point of interest. Only NPCs

880 with five or more subunits were considered for diameter measurement of NPCs. As

881 previously described [25], line segments were determined that connected opposing subunits for

882 each individual NPC. The NPC center was defined as the point to which the distance of all

883 line segments was minimal. The NPC radius was calculated as the distance from the center to

884 each subunit. Data was plotted using Prism9 software (Figure S3 C,D). Statistical

885 significance was tested using unpaired two-tailed t test in Prism9.

886   *NPC ring subunit template matching*

887   The obtained bin4 STA averages for CR, IR and NR were masked to only include a single

888   subunit and then used as search templates (lowpass filtered to 30 Å) to perform template

889   matching in full 3D-CTF-corrected bin4 tomograms with visible NPCs using GAPSTOP^{TM}

890   [https://gitlab.mpcdf.mpg.de/bturo/gapstop_tm] [42] based on the STOPGAP software package

891   [73]. The angular search range was set to a 6-degree sampling which has been shown to

892   increase TM performance [42]. The constrained cross-correlation (CCC) peaks which had

893   values 7x above the mean of the CCC-volume were extracted with their corresponding

894   orientations and then manually cleaned in the ArtiaX plugin [70] for ChimeraX [72] to obtain only

895   plausible candidates that are oriented correctly in the nuclear envelope. This resulted in three

896   different particle sets for CR, IR, NR with all template matched subunit coordinates and

897   orientations for each tomogram. The association of each ring subunit to individual NPCs was

898   determined using cryoCAT package [Turoňová, B. https://github.com/turonova/cryoCAT].

899

900   *NPC ring subunit interior angle of polygon (IAOP) measurements*

901   To obtain the interior angle of the polygon (IAOP) (see Figure 5C cartoon), i.e. the rotation

902   around the symmetry axis from a given to the neighboring subunit, in each NPC ring (CR, IR,

903   NR) an in-house python script was used. First, the circle center for each NPC ring was

904   determined using preexisting code [https://meshlogic.github.io/posts/jupyter/curve-

905   fitting/fitting-a-circle-to-cluster-of-3d-points/]. Here a threshold of at least four subunits per

906   NPC ring was used to ensure accurate circle fitting. Then the angle between neighboring

907   vectors connecting the circle center to the center of each subunit as determined by template

908   matching was calculated. To ensure that only the direct neighbor angles were measured a

909   threshold of 55° was applied and then only NPC rings with three or more angle

910   measurements were included in the final analysis. To determine statistical significance of the

911   measured angles in NPC rings between infected and control macrophages a threshold of

912   42.5° (the halfway point between the angle of a regular C8-symmetric NPC with 45° and the

913   angle of a C9-symmetric NPC with 40°) was chosen. Then the number of NPCs that had a

914   median subunit angle of less than 42.5° and those above or equal to the threshold were

915   extracted from the data and subjected to a Fisher's exact test (Prism 9 software). Data was

916   plotted using Python (Figure 5C, S4).

917   *In-situ capsid modeling*

918   A multi-step approach was employed to construct an atomic model of a complete *in situ* HIV

919   capsid. STA for hexamers and TM for pentamers applied to a single and relatively well-resolved

920   cone-shaped capsid yielded the centers of 141 hexamers and 8 pentamers (Figure S5A1,2).

921   From these, the capsid surface was estimated as a convex hull (Figure S5A3) using the ArtiaX

922   boundary method [70] in ChimeraX [72]. The position of missing points in the cone lattice were

923   then determined by oversampling random points on the surface of the convex hull and keeping

924   points closest to the expected positions based on the translation vectors of the existing

925   neighbors. Those with the most neighbors were iteratively selected, adding them one-by-one

926   to the list. Once complete, the positions of the 46 added lattice points (~24% of the total) were

927   visually inspected and manually adjusted in ChimeraX [72] (Figure S5A4).

928   In the next step, the lattice was globally relaxed by annealing a coarse-grained particle model

929   (Figure S5A5). Hexamers and pentamers were represented as beads. The six neighboring beads

930   of hexamers, and the five of pentamers were connected by harmonic springs $\kappa(r - r_0)^2/2$ with

931   r the pair distance, $r_0 = 9.3$ nm the distance between hexamers obtained by placing atomic

932   models [74],[75] in the experimental STA of the hexamer which included the first neighbor, and

933    $\kappa = 3$ kJ·mol^{-1}·nm^{-2} the spring constant. In addition, the beads were softly tethered to their

934   initial position by a potential $kd^2/2$ with d the distance and

935    $k = 1.0$ kJ·mol^{-1}·nm^{-2} the spring constant. The total energy was annealed using Gromacs 2022

936   [76] by reducing the temperature linearly from 300 K to 10 K in 10000 steps of molecular

937   dynamics.

938   Finally, the complete capsid was built by replacing each bead with atomic models of hexamers

939   (PDB ID: 8ckv [74]) and pentamers (PDB ID: 8g6l [75]) rotated and translated according to the

940   lattice (Figure S5A6). Missing loop residues were modeled using Swiss model [77].

941

942   *Coarse-grained model of NPC and HIV capsid*

943   We built coarse-grained models of the NPC and the HIV capsid in which each amino acid of

944   the proteins is mapped into a single particle [44]. The beads are categorized as protein residues

945   (p), membrane particles (m) and HIV capsid particles (c). The protein group has further sub-

946   categories: scaffold residues (sc) and FG residues (FG) of NPC proteins; outer (CA) and inner

947   (CA^i) residues of CA hexamers and CA pentamers building the HIV capsid; and the particles

948   containing inside the HIV capsid (HIV$_{in}$). The potential energy of the system was given by

$$U = U_{\text{LJ}} + U_{\text{FENE}} \qquad [1]$$

$$= 4k_B T \sum_{i<j, r_{ij}<r_c^\alpha, i,j \in p,m\}} \left\{ \tilde{\epsilon}_{ij} \left[\left(\frac{\sigma_{ij}}{r_{ij}}\right)^{12} - \left(\frac{\sigma_{ij}}{r_{ij}}\right)^6 \right] - U_{LJ}(r_c^\alpha) \right\}$$

$$+ 4k_B T \sum_{\langle i,j=i+1 \rangle, i,j \in p, r_{ij}<2^{\frac{1}{6}}\sigma} \left[\left(\frac{\sigma}{r_{ij}}\right)^{12} - \left(\frac{\sigma}{r_{ij}}\right)^6 + \frac{1}{4} \right]$$

$$- \sum_{\langle i,j=i+1 \rangle, \ i,j \in p} 0.5 k_{\text{FE}} R_{\text{FE}}^2 \ln \left[1 - \left(\frac{r_{ij}}{R_{FE}}\right)^2 \right]$$

949   The non-bonded interactions between particles i and j in all categories are modelled by

950   Lennard-Jones (LJ) potentials, whose strength $\tilde{\epsilon}_{ij}$, length σ_{ij}, and cut-off values r_c^α are listed

951   in Table S2A. The bond potential between neighboring beads along the FG-proteins is

952   expressed by the FENE potential [78] with $k_{\text{FE}} = 30 k_B T$ and $R_{\text{FE}} = 1.5\sigma$. All simulations were

953   performed in LAMMPS (Release date: Sept. 2021) [79]. Times are reported in units of $\tau =$

954   $\sqrt{m\sigma^2/k_B T}$, with m the bead mass. Box sizes are listed in Table S2B, and MD run lengths in

955   Table S2C.

956   A coarse-grained representation of the nuclear envelope separating the cytoplasm and

957   nucleoplasm was built as described [44]. We first built a tightly packed 100x100 nm² coarse-

958   grained POPC lipid bilayer patch (command: *insane.py -l POPC -x 100 -y 100 -z 100 -a 0.3 -*

959   *o bilayer.gro*). With this patch, we created a half-toroidal membrane pore using the BUMPy

960   software [80] (command: *bumpy.py -s double_bilayer_cylinder -f bilayer.gro -z 10 -g*

961   *l_cylinder:10 r_cylinder:550 r_junction:120 l_flat:2560*). We then placed particle beads at the

962   phosphate groups of the bilayer.

963   For the NPC, we used the dilated NPC based on PDB-ID: 7R5J [26] with the following FG-Nups

964   anchored as in model II of [44]: NUP54, NUP58, NUP62, NUP98, POM121, NUP214, NUP153

965   and NUP358. Both NPC scaffold and membrane particles were fixed during the simulations.

966   A LJ potential with large repulsive range prevented the escape of FG-Nups into the lumen of

967   the nuclear envelope (Table S2A). To match experiments [44], we set the FG-FG interaction

968   strength to $\tilde{\epsilon}_{\text{FG-FG}} = 0.42$ for all simulations unless otherwise stated. For $\tilde{\epsilon}_{\text{FG-FG}} = 0.42$, FG-

969   Nup98 (aa1-499) was found to be close to the critical point of protein condensate formation [44].

970   We confirmed that for $\tilde{\epsilon}_{\text{FG-FG}} = 0.42$ the FG-Nup98 root mean squared extension in the

971   dilated NPC structure used here agrees with the experimental FLIM-FRET measurements

972   (Figure S5C).

973

974 *Labelling the outer surface particles of HIV capsid*

975 In our model, FG-Nups bind only to the outer surface of the HIV capsid. To identify the outer

976 surface, we placed the coarse-grained HIV capsid inside a cubic box of size 441σ with 500

977 FG-Nup98 chains (aa1-499)) and ran MD simulations using a Langevin thermostat [81] with

978 damping coefficient 10τ. We treated the HIV capsid as a rigid body using a rigid body

979 integrator with a Langevin thermostat and a damping coefficient 3000τ (LAMMPS command:

980 *fix rigid langevin molecule*). With weak interaction strengths between FG-Nup and HIV capsid

981 particles, $\tilde{\epsilon}_{FG-FG} = \tilde{\epsilon}_{FG-CA} = 0.2$, the chains formed coil configurations and explored the outer

982 surface of HIV capsid. We did not observe the penetration of chains into the HIV capsid.

983 Particles within 1.5σ of the capsid were stored every 1000τ for $4.5 \times 10^5\tau$. We labelled an

984 HIV capsid particle as an outer particle if it contacted at least one FG-Nup particle during the

985 simulation. We then labelled all equivalent particles across the 182 CA hexamers and 12 CA

986 pentamers as outer particles, and all others as inner particles. We then filled the interior of the

987 capsid with "cargo," primarily RNA, modeled as particles on a cubic lattice (400807 particles

988 with lattice constant $\sigma_{lattice-lattice} = 2^{-\frac{1}{6}}\sigma$). Figure S5B shows the cut view of the HIV capsid

989 with inner lattice particles. We do not show the inner lattice particles in other figures.

990

991 *Binding affinity of a strand of FG-Nup153 to CA hexamers*

992 We estimated the effective FG-CA hexamer interaction strength by matching the calculated

993 binding affinity of a single CA hexamer and a fragment of FG-Nup153 to the experimentally

994 measured value [17]. A single CA hexamer and a 17-mer fragment of FG-Nup153 (aa1407-

995 aa1423) were simulated inside a cubic box of size $60\sigma = 36$ nm. We sampled the cross

996 interaction potential between CA hexamer and oligomer $U_{FG-CA}(t)$ every 10τ for $10^7\tau$, with

997 pair interactions truncated and shifted at 2σ. We defined CA hexamer and oligomer as bound

998 if the interacting energy was lower than the threshold energy: $U_{FG-CA} < U_{th}$. The probability

999 of the bound state was calculated as $P_b = \sum_{i=1}^{N} \frac{H(U_{th}-U_{FG-CA}(t_i))}{N}$, where $N = 10^6$ is the number

1000 of sampled energies, and $H(x) = 1$ for $x > 0$ and $H(x) = 0$ otherwise is the Heaviside

1001 function. The dissociation constant as a measure of the binding affinity is calculated as $K_d =$

1002 $\frac{(1-P_b)^2}{N_A V P_b}$, where N_A is the Avogadro number and $V = (36\text{nm})^3$ the box volume. As shown in

1003 Figure S5D,E, we found that for interaction strengths close to $\tilde{\epsilon}_{FG-CA} = 0.5$ the calculated

1004 binding affinity matches the experimental value $K_d^{exp} = 49\mu M$ [17] independent of threshold

1005 energy and damping coefficient of the Langevin thermostat.

1006 *Modelling cracks in NPC scaffold*

1007 We modelled a crack in the NPC scaffold by cutting its rings and pulling them apart at the seam

1008 to resemble a nine-fold symmetric scaffold. For this, the coordinates of scaffold beads in the

1009 cylindrical coordinate system $\{r, \theta, z\}$ were mapped into new coordinates $\{r_n, \theta_n, z_n\}$ according

1010 to

1011

$$r_{i,n} = \mathcal{R}\, r_i \qquad\qquad [2]$$

$$\theta_{i,n} = \begin{cases} \dfrac{8}{9}(\theta_i - \theta_0) + \dfrac{\pi}{9}, & \text{for } \theta_i > \theta_0 \\[2mm] \dfrac{8}{9}(\theta_i - \theta_0) + \dfrac{\pi}{9}, & \text{for } \theta_i < \theta_0 \end{cases}$$

$$z_{i,n} = z_i$$

1012 $\mathcal{R}$ is the radial scaling factor, θ_0 is the reference angle at which the NPC scaffold is cracked

1013 and the z coordinates of the beads are kept identical as in the intact NPC. This map retains the

1014 local interactions of the structure except at the crack. For scaling factors of $\mathcal{R} = 1.2$ and $\mathcal{R} =$

1015 1.45, the inner-ring diameters D_{in} widens from 58 nm to 69.6 nm and 84.1 nm, respectively.

1016 With $\theta_0 = 0.1031$ rad, we set the crack interface between two spokes of the NPC scaffold in

1017 our model. To fit the nuclear envelope around the new cracked NPC, we rescaled the radial

1018 coordinates of the membrane particles by factors 1.14 and 1.38 for $\mathcal{R} = 1.2$ and $\mathcal{R} = 1.45$,

1019 respectively. The resulting structures of the NPC scaffold are shown in Figure S6A-F.

1020 To model the dispersion in NPC diameters seen in the experiments (Figure S3D), we built intact

1021 NPC models with different scaffold pore dimensions. For this, we radially scaled the scaffold

1022 bead positions of the intact in-cell NPC without opening a lateral void by using the mapping

1023

$$r_{i,n} = \mathcal{R}\, r_i \qquad\qquad [3]$$

$$\theta_{i,n} = \theta_i$$

$$z_{i,n} = z_i$$

1024 To equilibrate the cracked and intact expanded NPCs, the FENE bond potential was initially

1025 replaced by a harmonic bond potential with $U_{har} = 0.5 k_{\text{harm}} \sum_{\langle i,j=i+1 \rangle,\ i,j \in p} 0.5 k_{har}\big(r_{ij} -$

1026 $\sigma\big)^2$, where $k_{\text{harm}} = 10^4 k_B T \sigma^{-2}$ and the sum runs over all bonded neighboring beads, i.e.

1027 $\langle i, j = i + 1 \rangle$. The systems were equilibrated for $131 \times 10^3 \tau$. Then the harmonic bonds were

1028 replaced with the FENE bond and the systems were equilibrated for at least $18 \times 10^3 \tau$.

1029

1030 *Force-driven passage of HIV capsid through NPC*

1031 We probed the passage of HIV capsids through NPCs in MD simulations with a force acting

1032 on the capsid pointing in a direction normal to the nuclear envelope. We aligned the long axis

1033 of the HIV capsid with the NPC symmetry axis. We placed the HIV capsid in the cytosol at a

1034 height of $z_i - z_C = -144$ nm of its center, where z_i is the NPC's inner-ring position. Then we

1035 applied a force $-\frac{10^{-3} k_B T}{\sigma} \approx -6.85 \times 10^{-3}$ pN directed along the z direction toward the

1036 nucleus onto each HIV capsid particle, amounting to a total force of 4.488 nN. The total

1037 simulation runs were $10^4 \, \tau$. For reference, we also simulated NPCs without FG-Nups. The

1038 position of the HIV capsid center as a function of the simulation time is shown in Figure S6G-

1039 L for three replicas. For the intact in-cell NPC ($D_{\text{in}} = 58$ nm), the HIV capsid remained stuck

1040 inside the NPC, with steric collisions blocking the translocation through the NPC scaffold even

1041 without FG-Nups. By contrast, the HIV capsid can translocate through the intact expanded

1042 NPC ($D_{\text{in}} = 69.9$ nm, $\mathcal{R} = 1.2$) and cracked NPCs ($D_{\text{in}} = 69.9$ nm, $\mathcal{R} = 1.2$ and $D_{\text{in}} = $

1043 84.1 nm, $\mathcal{R} = 1.45$).

1044

1045 *Free energy profile for HIV capsid passage through NPC*

1046 We used MD simulations to determine the free energy profile for HIV capsid passage through

1047 NPCs. We extracted a set of initial configurations at different capsid positions from the MD

1048 simulations of force-driven NPC passage described above. We then fixed the HIV capsid in

1049 space and ran simulations for $188 \times 10^3 \tau$. After $90 \times 10^3 \tau$ of equilibration, we averaged the

1050 total force on the HIV capsid directed along the z-axis every 10τ. Figures S7A-C show the

1051 final configurations for different HIV capsid positions along the translocation path. Figure S7D

1052 shows the total force on the HIV capsid per CA monomer (with a total of 1152 monomers in

1053 the HIV capsid). As described in the analysis of force-driven passage, steric clashes prevent

1054 the HIV capsid from translocating beyond $z_i - z_C > -10$ nm in the intact in-cell NPC. We

1055 obtained the potential of mean force by integrating the mean force along the translocation path,

1056 $\Delta F(z) = \int_{z_1}^{z} F_z(z) dz$, where z_1 is the initial position on the cytoplasmic side. For the intact in-

1057 cell NPC, numerical integration gave a free energy minimum at $z_i - z_C = -30.5$ nm. For the

1058 cracked NPCs with $D_{\text{in}} = 69.9$ nm and $D_{\text{in}} = 84.1$ nm, we fitted two Gaussian functions

1059 $F_z(z) = a_1 e^{-\left(\frac{z-b_1}{\sqrt{2}c_1}\right)^2} + a_2 e^{-\left(\frac{z-b_2}{\sqrt{2}c_2}\right)^2}$ to the force data with the symmetry constraint

1060 $\int_{-\infty}^{+\infty} F_z(z)dz = 0$. The fitting parameters are listed in Table S2D. For the cracked NPCs, the

1061 minima of the free energy are at $z_i - z_C = -1$ nm and 7 nm, respectively (Figure 6D).

1062

1063 *Release and tilt of HIV capsid inside NPC*

1064 The HIV capsid was released inside intact and cracked NPCs with $\tilde{\epsilon}_{FG-CA} = 0.5$. In MD

1065 simulations of at least 2×10^5 (Table S2C), the capsid position and orientation was relaxed.

1066 The final orientations of the released HIV capsids are shown in Figure 6E.

Data availability:

HIV capsid hexamer and pentamer maps reported in this paper will be deposited in the EMDB with accession codes XXX and released upon publication. The NPC maps will also be deposited in the EM Data Bank with accession codes XXX and released upon publication. The complete HIV capsid model used for simulations will be available at PDB-Dev with accession code XXX and released upon publication. The raw tilt series and alignment files for both HIV- and mock infected conditions will be deposited on EMPIAR with accession codes XXX and available upon publication. Initial configurations and trajectories of the MD simulations will be made available upon publication at zenodo.org under CC-BY license.

1094

Author contributions:

1096   J.P.K., V.Z., G.H., H.-G.K. and M.B. conceived the project. V.Z. designed and performed the

1097   fluorescence microscopy and CLEM experiments with help from V.L. and analyzed data.

1098   J.P.K. performed the cryo-ET data acquisition with help from S.W.. J.P.K. performed

1099   subtomogram averaging, template matching and subsequent data analysis with help from B.T.

1100   M.H. performed the MD simulations with help from S.C.-L. The manuscript was written by

1101   J.P.K., M.H., V.Z., G.H., H.-G.K. and M.B. A.O.-K. and J.K. provided important

1102   contributions to NPC structure analysis and statistical analysis respectively. All authors

1103   contributed to manuscript editing and approved the final manuscript.

1104

Competing interests:

1106   The authors declare no competing interests.

References

1. Yamashita, M., and Emerman, M. (2006). Retroviral infection of non-dividing cells: old and new perspectives. Virology *344*, 88–93.

2. Ananth, S., Ambiel, I., Schifferdecker, S., Müller, T.G., Wratil, P.R., Mejias-Perez, E., Kräusslich, H.G., Müller, B., Keppler, O.T., and Fackler, O.T. (2024). Spatial resolution of HIV-1 post-entry steps in resting CD4 T cells. Cell Rep *43*, 113941.

3. Dharan, A., Bachmann, N., Talley, S., Zwikelmaier, V., and Campbell, E.M. (2020). Nuclear pore blockade reveals that HIV-1 completes reverse transcription and uncoating in the nucleus. Nat Microbiol *5*, 1088–1095.

4. Müller, T.G., Zila, V., Peters, K., Schifferdecker, S., Stanic, M., Lucic, B., Laketa, V., Lusic, M., Müller, B., and Kräusslich, H.G. (2021). HIV-1 uncoating by release of viral cDNA from capsid-like structures in the nucleus of infected cells. eLife *10*, e64776.

5. Jang, S., and Engelman, A.N. (2023). Capsid–host interactions for HIV-1 ingress. Microbiol Mol Biol Rev *87*, 1.

6. Müller, T.G., Zila, V., Müller, B., and Kräusslich, H.G. (2022). Nuclear Capsid Uncoating and Reverse Transcription of HIV-1. Annu Rev Virol *9*, 261–284.

7. McDonald, D., Vodicka, M.A., Lucero, G., Svitkina, T.M., Borisy, G.G., Emerman, M., and Hope, T.J. (2002). Visualization of the intracellular behavior of HIV in living cells. J Cell Biol *159*, 441–452.

8. Badieyan, S., Lichon, D., Andreas, M.P., Gillies, J.P., Peng, W., Shi, J., DeSantis, M.E., Aiken, C.R., Böcking, T., Giessen, T.W., et al. (2023). HIV-1 binds dynein directly to hijack microtubule transport machinery. bioRxiv https://doi.org/10.1101/2023.08.29.555335.

9. Naghavi, M.H. (2021). HIV-1 capsid exploitation of the host microtubule cytoskeleton during early infection. Retrovirology *18*, 19.

10. Luban, J., Bossolt, K.L., Franke, E.K., Kalpana, G.V., and Goff, S.P. (1993). Human immunodeficiency virus type 1 Gag protein binds to cyclophilins A and B. Cell *73*, 1067–1078.

11. Gamble, T.R., Vajdos, F.F., Yoo, S., Worthylake, D.K., Houseweart, M., Sundquist, W.I., and Hill, C.P. (1996). Crystal structure of human cyclophilin A bound to the amino-terminal domain of HIV-1 capsid. Cell *87*, 1285–1294.

12. Dharan, A., Talley, S., Tripathi, A., Mamede, J.I., Majetschak, M., Hope, T.J., and Campbell, E.M. (2016). KIF5B and Nup358 Cooperatively Mediate the Nuclear Import of HIV-1 during Infection. PLoS Pathog *12*, e1005700.

13. Ganser, B.K., Li, S., Klishko, V.Y., Finch, J.T., and Sundquist, W.I. (1999). Assembly and analysis of conical models for the HIV-1 core. Science *283*, 80–83.

14. Zhao, G., Perilla, J.R., Yufenyuy, E.L., Meng, X., Chen, B., Ning, J., Ahn, J., Gronenborn, A.M., Schulten, K., Aiken, C., et al. (2013). Mature HIV-1 capsid structure by cryo-electron microscopy and all-atom molecular dynamics. Nature *497*, 643–646.

15. Mattei, S., Glass, B., Hagen, W.J.H., Kräusslich, H.-G., and Briggs, J.A.G. (2016). The structure and flexibility of conical HIV-1 capsids determined within intact virions. Science *354*, 1434–1437.

16. Matreyek, K.A., Yücel, S.S., Li, X., and Engelman, A. (2013). Nucleoporin NUP153 phenylalanine-glycine motifs engage a common binding pocket within the HIV-1 capsid protein to mediate lentiviral infectivity. PLoS Pathog *9*, e1003693.

17. Price, A.J., Jacques, D.A., McEwan, W.A., Fletcher, A.J., Essig, S., Chin, J.W., Halambage, U.D., Aiken, C., and James, L.C. (2014). Host cofactors and pharmacologic ligands share an essential interface in HIV-1 capsid that is lost upon disassembly. PLoS Pathog *10*, e1004459.

18. Yant, S.R., Mulato, A., Hansen, D., Tse, W.C., Niedziela-Majka, A., Zhang, J.R., Stepan, G.J., Jin, D., Wong, M.H., Perreira, J.M., et al. (2019). A highly potent long-acting small-molecule HIV-1 capsid inhibitor with efficacy in a humanized mouse model. Nat Med *25*, 1377–1384.

19. Bester, S.M., Wei, G., Zhao, H., Adu-Ampratwum, D., Iqbal, N., Courouble, V.V., Francis, A.C., Annamalai, A.S., Singh, P.K., Shkriabai, N., et al. (2020). Structural and mechanistic bases for a potent HIV-1 capsid inhibitor. Science *370*, 360–364.

20. Bejarano, D.A., Peng, K., Laketa, V., Börner, K., Jost, K.L., Lucic, B., Glass, B., Lusic, M., Müller, B., and Kräusslich, H.G. (2019). HIV-1 nuclear import in macrophages is regulated by CPSF6-capsid interactions at the nuclear pore complex. eLife 8, e41800.

21. von Appen, A., Kosinski, J., Sparks, L., Ori, A., DiGuilio, A.L., Vollmer, B., Mackmull, M.T., Banterle, N., Parca, L., Kastritis, P., et al. (2015). In situ structural analysis of the human nuclear pore complex. Nature 526, 140–143.

22. Francis, A.C., and Melikyan, G.B. (2018). Single HIV-1 Imaging Reveals Progression of Infection through CA-Dependent Steps of Docking at the Nuclear Pore, Uncoating, and Nuclear Transport. Cell Host Microbe 23, 536–548.e6.

23. Zila, V., Margiotta, E., Turoňová, B., Müller, T.G., Zimmerli, C.E., Mattei, S., Allegretti, M., Börner, K., Rada, J., Müller, B., et al. (2021). Cone-shaped HIV-1 capsids are transported through intact nuclear pores. Cell 184, 1032–1046.e18.

24. Schifferdecker, S., Zila, V., Müller, T.G., Sakin, V., Anders-Össwein, M., Laketa, V., Kräusslich, H.G., and Müller, B. (2022). Direct Capsid Labeling of Infectious HIV-1 by Genetic Code Expansion Allows Detection of Largely Complete Nuclear Capsids and Suggests Nuclear Entry of HIV-1 Complexes via Common Routes. mBio 13, e0195922.

25. Zimmerli, C.E., Allegretti, M., Rantos, V., Goetz, S.K., Obarska-Kosinska, A., Zagoriy, I., Halavatyi, A., Hummer, G., Mahamid, J., Kosinski, J., et al. (2021). Nuclear pores dilate and constrict in cellulo. Science 374, eabd9776.

26. Mosalaganti, S., Obarska-Kosinska, A., Siggel, M., Taniguchi, R., Turoňová, B., Zimmerli, C.E., Buczak, K., Schmidt, F.H., Margiotta, E., Mackmull, M.T., et al. (2022). AI-based structure prediction empowers integrative structural analysis of human nuclear pores. Science 376, eabm9506.

27. Mahamid, J., Pfeffer, S., Schaffer, M., Villa, E., Danev, R., Cuellar, L.K., Förster, F., Hyman, A.A., Plitzko, J.M., and Baumeister, W. (2016). Visualizing the molecular sociology at the HeLa cell nuclear periphery. Science 351, 969–972.

28. Schuller, A.P., Wojtynek, M., Mankus, D., Tatli, M., Kronenberg-Tenga, R., Regmi, S.G., Dip, P.V., Lytton-Jean, A.K.R., Brignole, E.J., Dasso, M., et al. (2021). The cellular environment shapes the nuclear pore complex architecture. Nature 598, 667–671.

29. Petrovic, S., Samanta, D., Perriches, T., Bley, C.J., Thierbach, K., Brown, B., Nie, S., Mobbs, G.W., Stevens, T.A., Liu, X., et al. (2022). Architecture of the linker-scaffold in the nuclear pore. Science 376, eabm9798.

30. Görlich, D., and Kutay, U. (1999). Transport Between the Cell Nucleus and the Cytoplasm. Annual Review of Cell and Developmental Biology 15, 607–660.

31. Shen, Q., Feng, Q., Wu, C., Xiong, Q., Tian, T., Yuan, S., Shi, J., Bedwell, G.J., Yang, R., Aiken, C., et al. (2023). Modeling HIV-1 nuclear entry with nucleoporin-gated DNA-origami channels. Nat Struct Mol Biol 30, 425–435.

32. Fu, L., Weiskopf, E.N., Akkermans, O., Swanson, N.A., Cheng, S., Schwartz, T.U., and Görlich, D. (2024). HIV-1 capsids enter the FG phase of nuclear pores like a transport receptor. Nature 626, 843–851.

33. Dickson, C.F., Hertel, S., Tuckwell, A.J., Li, N., Ruan, J., Al-Izzi, S.C., Ariotti, N., Sierecki, E., Gambin, Y., Morris, R.G., et al. (2024). The HIV capsid mimics karyopherin engagement of FG-nucleoporins. Nature 626, 836–842.

34. Einkauf, K.B., Lee, G.Q., Gao, C., Sharaf, R., Sun, X., Hua, S., Chen, S.M., Jiang, C., Lian, X., Chowdhury, F.Z., et al. (2019). Intact HIV-1 proviruses accumulate at distinct chromosomal positions during prolonged antiretroviral therapy. J Clin Invest 129, 988–998.

35. Lusic, M., and Siliciano, R.F. (2017). Nuclear landscape of HIV-1 infection and integration. Nat Rev Microbiol 15, 69–82.

36. Deshpande, A., Bryer, A.J., Andino, J., Shi, J., Hong, J., Torres, C., Harel, S., Francis, A.C., Perilla, J.R., Aiken, C., et al. (2023). Elasticity of the HIV-1 Core Facilitates Nuclear Entry and Infection. bioRxiv https://doi.org/10.1101/2023.09.29.560083.

37. Thevathasan, J.V., Kahnwald, M., Cieśliński, K., Hoess, P., Peneti, S.K., Reitberger, M., Heid, D., Kasuba, K.C., Hoerner, S.J., Li, Y., et al. (2019). Nuclear pores as versatile reference standards for quantitative superresolution microscopy. Nat Methods 16, 1045–1053.

38. Briggs, J.A., Wilk, T., Welker, R., Kräusslich, H.G., and Fuller, S.D. (2003). Structural organization of authentic, mature HIV-1 virions and cores. EMBO J *22*, 1707–1715.

39. Briggs, J.A., Grünewald, K., Glass, B., Förster, F., Kräusslich, H.G., and Fuller, S.D. (2006). The mechanism of HIV-1 core assembly: insights from three-dimensional reconstructions of authentic virions. Structure *14*, 15–20.

40. Ni, T., Zhu, Y., Yang, Z., Xu, C., Chaban, Y., Nesterova, T., Ning, J., Böcking, T., Parker, M.W., Monnie, C., et al. (2021). Structure of native HIV-1 cores and their interactions with IP6 and CypA. Sci Adv *7*, eabj5715.

41. Hudait, A., and Voth, G.A. (2024). HIV-1 capsid shape, orientation, and entropic elasticity regulate translocation into the nuclear pore complex. Proc Natl Acad Sci U S A *121*, e2313737121.

42. Cruz-León, S., Majtner, T., Hoffmann, P.C., Kreysing, J.P., Kehl, S., Tuijtel, M.W., Schaefer, S.L., Geißler, K., Beck, M., Turoňová, B., and Hummer, G. (2023). High-confidence 3D template matching for cryo-electron tomography. Nat Commun, in press https://doi.org/10.1038/s41467-024-47839-8

43. Taniguchi, R., Orniacki, C., Kreysing, J.P., Zila, V., Zimmerli, C.E., Böhm, S., Turoňová, B., Kräusslich, H.-G., Doye, V., and Beck, M. (2024). Nuclear pores safeguard the integrity of the nuclear envelope. bioRxiv https://doi.org/10.1101/2024.02.05.578890.

44. Yu, M., Heidari, M., Mikhaleva, S., Tan, P.S., Mingu, S., Ruan, H., Reinkemeier, C.D., Obarska-Kosinska, A., Siggel, M., Beck, M., et al. (2023). Visualizing the disordered nuclear transport machinery in situ. Nature *617*, 162–169.

45. Humphrey, W., Dalke, A., and Schulten, K. (1996). VMD: visual molecular dynamics. J Mol Graph *14*, 33–8, 27.

46. Bhattacharya, A., Alam, S.L., Fricke, T., Zadrozny, K., Sedzicki, J., Taylor, A.B., Demeler, B., Pornillos, O., Ganser-Pornillos, B.K., Diaz-Griffero, F., et al. (2014). Structural basis of HIV-1 capsid recognition by PF74 and CPSF6. Proc Natl Acad Sci U S A *111*, 18625–18630.

47. Hoffmann, P.C., Kim, H., Obarska-Kosinska, A., Kreysing, J.P., Andino-Frydman, E., Cruz-Leon, S., Cernikova, L., Kosinski, J., Turoňová, B., Hummer, G., et al. (2024). Nuclear pores as conduits for fluid flow during osmotic stress. bioRxiv https://doi.org/10.1101/2024.01.17.575985.

48. Zoldák, G., and Rief, M. (2013). Force as a single molecule probe of multidimensional protein energy landscapes. Curr Opin Struct Biol *23*, 48–57.

49. Hinshaw, J.E., and Milligan, R.A. (2003). Nuclear pore complexes exceeding eightfold rotational symmetry. J Struct Biol *141*, 259–268.

50. Pear, W.S., Nolan, G.P., Scott, M.L., and Baltimore, D. (1993). Production of high-titer helper-free retroviruses by transient transfection. Proc Natl Acad Sci U S A *90*, 8392–8396.

51. Adachi, A., Gendelman, H.E., Koenig, S., Folks, T., Willey, R., Rabson, A., and Martin, M.A. (1986). Production of acquired immunodeficiency syndrome-associated retrovirus in human and nonhuman cells transfected with an infectious molecular clone. J Virol *59*, 284–291.

52. Schnell, G., Joseph, S., Spudich, S., Price, R.W., and Swanstrom, R. (2011). HIV-1 replication in the central nervous system occurs in two distinct cell types. PLoS Pathog *7*, e1002286.

53. Albanese, A., Arosio, D., Terreni, M., and Cereseto, A. (2008). HIV-1 pre-integration complexes selectively target decondensed chromatin in the nuclear periphery. PLoS One *3*, e2413.

54. Welker, R., Hohenberg, H., Tessmer, U., Huckhagel, C., and Kräusslich, H.G. (2000). Biochemical and structural analysis of isolated mature cores of human immunodeficiency virus type 1. J Virol *74*, 1168–1177.

55. Pizzato, M., Erlwein, O., Bonsall, D., Kaye, S., Muir, D., and McClure, M.O. (2009). A one-step SYBR Green I-based product-enhanced reverse transcriptase assay for the quantitation of retroviruses in cell culture supernatants. J Virol Methods *156*, 1–7.

56. Staudt, T., Engler, A., Rittweger, E., Harke, B., Engelhardt, J., and Hell, S.W. (2011). Far-field optical nanoscopy with reduced number of state transition cycles. Opt Express *19*, 5644–5657.

57. de Chaumont, F., Dallongeville, S., Chenouard, N., Hervé, N., Pop, S., Provoost, T., Meas-Yedid, V., Pankajakshan, P., Lecomte, T., Le Montagner, Y., et al. (2012). Icy: an open bioimage informatics platform for extended reproducible research. Nat Methods *9*, 690–696.

58. Schindelin, J., Arganda-Carreras, I., Frise, E., Kaynig, V., Longair, M., Pietzsch, T., Preibisch, S., Rueden, C., Saalfeld, S., Schmid, B., et al. (2012). Fiji: an open-source platform for biological-image analysis. Nat Methods *9*, 676–682.

59. Kukulski, W., Schorb, M., Welsch, S., Picco, A., Kaksonen, M., and Briggs, J.A. (2011). Correlated fluorescence and 3D electron microscopy with high sensitivity and spatial precision. J Cell Biol *192*, 111–119.

60. Mastronarde, D.N. (2005). Automated electron microscope tomography using robust prediction of specimen movements. Journal of Structural Biology *152*, 36–51.

61. Schorb, M., Gaechter, L., Avinoam, O., Sieckmann, F., Clarke, M., Bebeacua, C., Bykov, Y.S., Sonnen, A.F., Lihl, R., and Briggs, J.A.G. (2017). New hardware and workflows for semi-automated correlative cryo-fluorescence and cryo-electron microscopy/tomography. J Struct Biol *197*, 83–93.

62. Kremer, J.R., Mastronarde, D.N., and McIntosh, J.R. (1996). Computer visualization of three-dimensional image data using IMOD. J Struct Biol *116*, 71–76.

63. Paul-Gilloteaux, P., Heiligenstein, X., Belle, M., Domart, M.C., Larijani, B., Collinson, L., Raposo, G., and Salamero, J. (2017). eC-CLEM: flexible multidimensional registration software for correlative microscopies. Nat Methods *14*, 102–103.

64. Schaffer, M., Engel, B.D., Laugks, T., Mahamid, J., Plitzko, J.M., and Baumeister, W. (2015). Cryo-focused Ion Beam Sample Preparation for Imaging Vitreous Cells by Cryo-electron Tomography. Bio Protoc *5*, e1575.

65. Hagen, W.J.H., Wan, W., and Briggs, J.A.G. (2017). Implementation of a cryo-electron tomography tilt-scheme optimized for high resolution subtomogram averaging. J Struct Biol *197*, 191–198.

66. Grant, T., and Grigorieff, N. (2015). Measuring the optimal exposure for single particle cryo-EM using a 2.6 Å reconstruction of rotavirus VP6. eLife *4*, e06980.

67. Wan, W., Kolesnikova, L., Clarke, M., Koehler, A., Noda, T., Becker, S., and Briggs, J.A.G. (2017). Structure and assembly of the Ebola virus nucleocapsid. Nature *551*, 394–397.

68. Zheng, S., Wolff, G., Greenan, G., Chen, Z., Faas, F.G.A., Bárcena, M., Koster, A.J., Cheng, Y., and Agard, D.A. (2022). AreTomo: An integrated software package for automated marker-free, motion-corrected cryo-electron tomographic alignment and reconstruction. J Struct Biol X *6*, 100068.

69. Turoňová, B., Schur, F.K.M., Wan, W., and Briggs, J.A.G. (2017). Efficient 3D-CTF correction for cryo-electron tomography using NovaCTF improves subtomogram averaging resolution to 3.4Å. J Struct Biol *199*, 187–195.

70. Ermel, U.H., Arghittu, S.M., and Frangakis, A.S. (2022). ArtiaX: An electron tomography toolbox for the interactive handling of sub-tomograms in UCSF ChimeraX. Protein Sci *31*, e4472.

71. Allegretti, M., Zimmerli, C.E., Rantos, V., Wilfling, F., Ronchi, P., Fung, H.K.H., Lee, C.W., Hagen, W., Turoňová, B., Karius, K., et al. (2020). In-cell architecture of the nuclear pore and snapshots of its turnover. Nature *586*, 796–800.

72. Goddard, T.D., Huang, C.C., Meng, E.C., Pettersen, E.F., Couch, G.S., Morris, J.H., and Ferrin, T.E. (2018). UCSF ChimeraX: Meeting modern challenges in visualization and analysis. Protein Sci *27*, 14–25.

73. Wan, W., Khavnekar, S., and Wagner, J. (2023). STOPGAP, an open-source package for template matching, subtomogram alignment, and classification. bioRxiv https://doi.org/10.1101/2023.12.20.572665.

74. Stacey, J.C.V., Tan, A., Lu, J.M., James, L.C., Dick, R.A., and Briggs, J.A.G. (2023). Two structural switches in HIV-1 capsid regulate capsid curvature and host factor binding. Proc Natl Acad Sci U S A *120*, e2220557120.

75. Highland, C.M., Tan, A., Ricaña, C.L., Briggs, J.A.G., and Dick, R.A. (2023). Structural insights into HIV-1 polyanion-dependent capsid lattice formation revealed by single particle cryo-EM. Proc Natl Acad Sci U S A *120*, e2220545120.

76. Abraham, M.J., Murtola, T., Schulz, R., Páll, S., Smith, J.C., Hess, B., and Lindahl, E. (2015). GROMACS: High performance molecular simulations through multi-level parallelism from laptops to supercomputers. SoftwareX *1-2*, 19–25.

77. Waterhouse, A., Bertoni, M., Bienert, S., Studer, G., Tauriello, G., Gumienny, R., Heer, F.T., de Beer, T.A.P., Rempfer, C., Bordoli, L., et al. (2018). SWISS-MODEL: homology modelling of protein structures and complexes. Nucleic Acids Res *46*, W296–W303.

78. Kremer, K., and Grest, G.S. (1990). Dynamics of entangled linear polymer melts: A molecular-dynamics simulation. J Chem Phys *92*, 5057–5086.

79. Plimpton, S. (1995). Fast Parallel Algorithms for Short-Range Molecular Dynamics. Journal of Computational Physics *117*, 1–19.

80. Boyd, K.J., and May, E.R. (2018). BUMPy: A Model-Independent Tool for Constructing Lipid Bilayers of Varying Curvature and Composition. J Chem Theory Comput *14*, 6642–6652.

81. Dünweg, B., and Paul, W. (1991). Brownian Dynamics Simulations Without Gaussian Random Numbers. Int J Mod Phys C *02*, 817–827.